Mineralogical, Elemental, and Spatial Variability of Volcaniclastics in Fluvio-Coastal-Aeolian Sedimentary Systems and Their Insights for Mineral Sorting on Mars

Ignatius Argadestya[1], Abduljamiu O. Amao[1] , Candice C. Bedford[2,3], Pantelis Soupios[1] and Khalid Al-Ramadan[1]

[1]College of Petroleum Engineering and Geosciences, King Fahd University of Petroleum and Minerals, P.O. Box 5061, Dhahran - 31261, Saudi Arabia.

[2] Lunar and Planetary Institute, Universities Space Research Association, 3600 Bay Area Blvd., Houston, TX, USA.

[3] Astromaterials Research and Exploration Science, NASA Johnson Space Center, Houston, TX, USA.

Corresponding author: Ignatius Argadestya (g201706790@kfupm.edu.sa)

Key Points:

- Volcanic cyclic eruption, fluvial discharge, longshore current, and coastal volcaniclastic aeolian sand dunes are all inseparable from shaping the geomorphology of a reworked volcaniclastic terrain in Merapi sedimentary systems.
- Mineral sorting variability can be observed in bedforms regardless of its grain size distribution and the depositional environment of its sedimentary system.
- Wind-driven sorting in aeolian environment shows both mineralogical and average grain size function are gradually changing across the bedforms, parallel to the direction of prevailing wind, despite having similar average grain size.
- Chemical alteration index supports the hypotheses of Gale Crater's fluvially-transported Stimson formation and aqueous-driven alteration of Murray formation on Mars.

Abstract

This study investigates the mineralogical, elemental, and spatial variability from source (proximal) to sink (distal) of Merapi basalt-andesitic stratovolcano (Java, Indonesia) to better constrain volcaniclastic mineral sorting in fluvial, aeolian, and coastal environments. Merapi volcaniclastics are products of an active volcano with an ongoing quadrennial eruption, which can provide insights to constrain Mars' older and more recent volcaniclastics by focusing on anorthite, albite, and pyroxenes found on Mars' crust. We collected stream sediment samples across the Opak River that connects Merapi with the Indian Ocean and acquired Ground Penetrating Radar (GPR) surveys on Parangkusumo Shoreface and a parabolic coastal sand dune. In addition to grain size separation, all collected samples were subjected to X-Ray Diffractometer (XRD) and X-Ray Fluorescence (XRF) to quantify their mineralogical and elemental composition,

respectively, like the techniques used by the Curiosity rover on Mars to investigate the geochemistry and mineralogy of geological units in the Gale crater. To interpret the geochemical analysis, we applied multivariate statistical analysis based on Principal Component Analysis (PCA) and Hierarchical Clustering of Principal Component (HCPC). The quantitative assessment shows that the provenance contains pyroclastic materials dominated by plagioclase feldspars (albite and anorthite), followed by pyroxenes (augite and enstatite), similar to the findings of basalt-andesitic minerals on Mars' Gale and Gusev Crater. Mineral sorting from Merapi volcaniclastics shows a plagioclase feldspar sorting from proximal to the proximal-medial interface, fault-influenced pyroxene sorting from medial to distal, and pyroxene sorting in the aeolian-dominated sedimentary system.

Keywords: Volcaniclastic; Fluvial; Coastal; Aeolian; Parabolic Dune; Mars; Mineralogy; Pyroclastic Flow; Planetary Science

Plain Language Summary

This research provides a detailed characterization of stream samples and surface deposits from the Opak River, the Parangkusumo Shoreface, and parabolic coastal sand dunes from an active Merapi stratovolcano (Java, Indonesia) transported from the source towards the sink. The paper aims to constrain pyroclastic mineral sorting from a basaltic to basalt-andesitic volcanic origin throughout fluvial, coastal, and wind-driven (aeolian) environments. We use similar methods as the MSL (Mars Science Laboratory) Team to investigate mineral sorting of volcaniclastic sediments in Gale Crater, specifically using X-Ray spectroscopy collected by CheMin and ChemCam. In addition, we also acquired Ground Penetrating Radar (GPR) profiles along the volcaniclastic dune to provide an insight for the Mars' Perseverance RIMFAX GPR instrument. The results of our research suggest that mineralogical sorting occurs throughout the depositional subenvironments, and they are related to the geomorphology of the river. Furthermore, the aeolian environment provides an additional sorting mechanism for the sand grains deposited in the shoreface. We also discovered a similar weathering trend of Merapi volcanic sediments with the findings from Stimson and Murray formation in Gale Crater, which supports their result as sediment transported by the river back when the surface of Mars could sustain running water.

1 Introduction

Volcaniclastic dunes of reworked igneous materials are relatively less abundant on Earth as they require volcanic deposits to source the sand dunes. Java Island in Indonesia offers a natural laboratory for volcaniclastic sedimentary systems thanks to abundant active volcanoes formed within the island, offering observable volcaniclastic materials deposition from source (proximal) to sink (distal) area. We select Merapi stratovolcano for its basaltic to basalt-andesitic pyroclastic materials (Lorenz, 1974; Berthommier and Camus, 1991; Andreastuti et al., 2000; Camus et al., 2000; Voight et al., 2000; Charbonnier and Gertisser,

2008; Surono et al., 2012), with similar mineralogy dominated by feldspar and pyroxene of reworked igneous origin detected at Gale Crater (Schmidt et al., 2014; Treiman et al., 2016; Siebach et al., 2017; Bedford et al., 2020; Payré et al., 2020; Rampe et al., 2020) and Gusev Crater's Home Plate on Mars (Squyres et al., 2007). Previous studies of Merapi pyroclastics' mineralogical and elemental composition stated previously focused on the proximal setting, which leaves a gap in understanding how these deposits accumulate along their respective environments that eventually source the volcaniclastic dunes at the distal area. This study will fill the gap by investigating Merapi pyroclastics (proximal), Opak River channel bar deposits (medial - distal), Opak Estuary, Parangkusumo Shoreface, and the parabolic coastal sand dune (distal).

Merapi and its subsequent depositional environments represent an interaction between volcanic, fluvial, coastal, and aeolian sedimentary systems. Very few have looked into how volcaniclastic materials from more evolved volcanism and explosive volcanism is incorporated into these systems, despite its increasing evidence in the Mars geological record. Similar depositional environments are detected on Mars that Merapi volcano can provide valuable insights, such as: (1) Pyroclastic flow deposits (Brož and Hauber, 2012) identified at Tyrrhena Patera (Gregg and Farley, 2006) and Home Plate, Gusev Crater (Squyres et al., 2007); (2) Fluvial and aeolian sediments on Mars (Greeley et al., 1992; Fassett and Head, 2005; Grotzinger et al., 2005; Carr, 2012; Schmidt et al., 2014; Lapotre and Rampe, 2018; Payré et al., 2020); (3) The initiation of fluvial valleys on martian volcano (Gulick and Baker, 1990; Alemanno, 2018), and the missing link between fluvial and aeolian sediments of transported reworked igneous provenance in building up volcaniclastic aeolian dunes (Hooper et al., 2012); (4) A possible Northern lowlands paleo-coastline (Carr and Head, 2003), and (5) Mineral sorting on Mars sedimentary systems, such as the provenance study of Bradbury Group (Siebach et al., 2017; Bedford et al., 2019), and the hypothesis of the source and mineral sorting in Murray formation (Mangold et al., 2019) and Stimson formation, Gale Crater (Bedford et al., 2020; Rampe et al., 2020). These previous studies established the basis of our quantitative assessment to target specific minerals and elements from source to sink of Merapi volcaniclastic sedimentary systems, in conjunction of further insights for Mars volcaniclastics that can be observed from our study.

Mars possesses a diverse sedimentary record indicating that rivers, lakes, glaciers, and potentially oceans existed in the past before its climate transitioned to the dry and aeolian-dominated sedimentary environments of today (Greeley et al., 1992; Edgett and Lancaster, 1993; Fassett and Head, 2005; Squyres et al., 2007; Carr, 2012; Hooper et al., 2012; Grotzinger et al., 2014; Schmidt et al., 2014; Alemanno, 2018). In particular, Mars' sedimentary units deposited in fluviolacustrine settings have been targeted for in-situ investigations with rover and lander spacecraft such as the NASA Mars 2020 Perseverance rover (Jezero crater, 2021) and the NASA Curiosity rover (Gale crater, 2012). To date, most Mars-like Earth mineralogical studies focus on basaltic environments, but with the results from the Curiosity rover, it suggests

that the Mars analog literature should be expanded to include evolved igneous provenances. Regardless, most Gale crater sediments contain high abundances of feldspar, with varying abundances of pyroxene (Rampe et al., 2020). As such, we will focus on the sorting of these minerals in the fluvial and aeolian sedimentary environments on Merapi and discuss their implications for sorting in Mars sedimentary systems.

2 Methodology

This research investigates the interaction between volcanic eruption, pyroclastic flow, and fluvial-coastal-aeolian systems through geological field observation, followed by geophysical, geochemical, and multivariate statistical analysis to interpret the mineralogical and elemental compositions along with their depositional environments.

2.1 Geological Settings

Mount Merapi is an active stratovolcano formed as a result of the Java subduction zone where the Indo-Australian Plate is subducting under the Sunda Plate at a convergence rate of 6.7 cm/year (Kopp et al., 2006). Merapi volcanic eruptions are quadrennial, typically recurring every 4 to 6 years in their current state (Andreastuti et al., 2000; Voight et al., 2000; Surono et al., 2012). Volcaniclastic materials with a high amount of basaltic-andesite tephra, pyroclastic flow, viscous andesitic lava, and lahar are recorded as the main products of its eruption in the source (proximal) area (Lorenz, 1974; Camus et al., 2000; Surono et al., 2012). Lahar flows carve channels that are subsequently used by both pyroclastic flows and tributaries of Opak River (Lavigne et al., 2000). Opak River initially flows in SE direction from proximal – medial (0 – 20 km), and eventually in SW direction during medial – distal (20 – 45 km), shown in Fig. 1A. Merapi's modern eruption material is recorded with lithological unit Qmi throughout the study area (Fig. 1B). Opak River forms Opak Estuary before discharging into the Indian Ocean (Fig. 2A). The NE-SW motion of Opak River's discharge creates a tidal inlet (Fig. 2B) within the washover barrier sand (Fig. 2C). Sediments deposited on the estuary are transported further by the longshore current across Parangkusumo Shoreface, which supplied the backshore's parabolic sand dunes (Ray et al., 2005). These dunes are situated 300 m northward from the foreshore, with heights reaching up to 6-7 m (Fig. 2D), and their lee side is dominated by vegetation in form of shrubs. We select one dune in this research since it is the only publicly available to conduct our work. Despite the limitation, the parabolic sand dune that we select is representative as other dunes are similar in their overall geometry (e.g. their arc concaving against the prevailing NW wind, dark to light grey-colored sand, and shrubs on their lee-side) (Fig. 2D).

2.2 Sampling and Processing

Two GPR profiles were acquired to identify the internal structure of the shoreface and a parabolic sand dune using GSSI SIR 4000 installed with 100 Mhz antennae. A 110 m long GPR profile (Fig. 3A) is acquired on our

selected dune with surface sediment sampling along its blowout surface, stoss, and lee (Fig. 3B). Similarly, we acquired a 90 m GPR profile (Fig. 3C) on Parangkusumo Shoreface along with surface sediment sampling from the foreshore, berm, and backshore. Post-processing for both GPR lines includes global background removal, time-zero, first break estimation, predictive deconvolution, wavenumber filtering, amplitude and power gain, and topographic correction. An additional motivation to perform this method is Mars rover Perseverance is also equipped with a built-in GPR called RIMFAX (Radar Imager for Mars' Subsurface Experiment; Hamran et al., 2020), and ESA EXOMARS has a payload called WISDOM (Water Ice and Subsurface Deposit Observations on Mars; Hervé et al., 2020) which can yield non-destructive geophysical investigation on any planetary surface body (Ciarletti et al., 2007).

Stream sediment sampling follows the USGS field method for fluvial sediment measurement (Edwards & Glysson, 1999), with select sampling locations chosen according to the type of bars present (Fig. 4A). Stream sediment samples were collected by scooping the top surface deposit regardless of their grain size, then stored in a 100 ml airtight vial. Sampling locations were plotted with elevation and distance from source to sink (Fig. 4B). The samples were then dried in a vacuum oven at a temperature of 60°C for 24 hours to remove any fluids (water and brine). Details for each collected sample are presented in Table 1.

To separate the grain size distribution, 25 g aliquots of each sample were sieved with a rotary shaker for 10 minutes. 6 sieving racks stacked with phi number ( ) ranging from 0 to +4 represent very coarse - very fine sand, whereas +5 and >6 represent coarse - medium and medium - fine silt. We estimated the average grain size by multiplying the result from sieve analysis (Fig. 6) with the grain size category (phi number), which will give a function of grain size relative to each sample net weight percentage. Bulk samples for XRD and XRF were pulverized prior to analyses using a rock crusher machine for 15 minutes. The bulk mineral abundance was identified with XRD (Panalytical Empyrean X-Ray Diffractometer) through two measurements performed per sample, and the results were tabulated as averages, calculated according to the average value for each peak in the spectrum (Table 2). For the determination of major and minor bulk elemental concentrations, samples were first pulverized into powder, loaded into special cups and the analysed on a MicroXRF setup (BRUKER M4 Tornado), equipped with a polycarpellary optic (~20- m spot-size) and a micro-focused rhodium source operated at 50 kV and 600 A. The system employs two silicon-drift detectors to collect fluorescence spectra from the specimen under vacuum (20 mbar). Elemental spectra for individual atomic species were generated using the proprietary M4 software package. To ensure repeatability and data robustness, the entire sample surfaces were scanned with an X-ray beam capable of penetrating up to ~2 mm into the sample from the surface. Each sample was scanned in triplicate to ensure the results are reproduceable and after which the mean values were taken. In addition, the MicroXRF instrument is calibrated based on NIST 620 soda-lime glass reference material. Major and minor elemental concentration were also validated against the following certified

reference materials (LGC 2700, CGL 002, SRM 41, CGL 010) before the commencement of analysis. Instrument stability and accuracy are well documented (Kaufhold et al., 2016; Raschke et al., 2013; Rodriguez et al., 2005) The principle of position-tagged spectroscopy guides the elemental distribution mapping of the samples. Data obtained were stored in a three-dimensional data cube (X-Y-Z), where X and Y represent coordinates and Z, the fluorescence spectrum of each pixel. This allows for later retrieval and post-processing of various 2D rendering combinations of elements in defined regions of interest.

We selected hand specimen samples (Table 1) as host rocks and calculated their average pyroxene/plagioclase feldspar ratio (Px/PF) as a cut-off value to determine the mineralogical sorting against their depositional environment (Fig. 8). We combined the average grain size value (Fig. 6) with the Px/PF ratio (Fig. 8) to identify the relationship between mineral sorting against the grain size function and its subsequent depositional distance (Fig. 9). Subsequently, we discriminated the stream sediment samples as pre-fault fluvial and post-fault fluvial in order to understand the significance of Opak River in altering the mineralogical and grain size sorting (Fig. 9A). We calculated the average Px/PF ratio of parabolic sand dunes and compare it with Px/PF ratio of modern (Rocknest, Gobabeb, Ogunquit Beach) and ancient aeolian on Mars (Stimson formation's Big Sky, Okoruso, Greenhorn, and Lubango) (Fig. 9B). The pyroxene of Stimson formation was summed values from pigeonite and orthopyroxene (Rampe et al., 2020). We calculated the Chemical Index of Alteration (CIA, in molar proportions) based on the measured oxides from the XRF. We converted the wt% into molar by dividing the weight percent by molecular weight (Goldberg and Humayun, 2010). We used the CIA ratio (Nesbitt and Young, 1982) as follows: CIA = (Al_2O_3 / Al_2O_3 + CaO* + Na_2O + K_2O) x 100 whereas the CaO is derived from silicates' Ca content. We compiled the molar values from our findings to plot A-CN-K ternary diagram (Fig. 12) along with findings from Gale Crater (Mangold et al., 2019), Stimson formation (Bedford et al., 2020), and Mars' crust (Taylor and McLennan, 2009). The wt% and molar conversion of our data are available in supplementary data.

2.3 Multivariate Statistical Analysis

In order to reduce the relative effects of variables measured on different instruments, scales and ranges, the datasets we obtained from XRD and XRF were all scaled and centered; that is, by subtracting each variable's mean from its individual score and then dividing by the variable's standard deviation. This linear transformation does not alter the correlations among the variables, and it is often recommended (Hussain et al., 2018). We employed two multivariate statistical techniques to find patterns in our high dimensional dataset and establish relationships. First, we implemented Principal Component Analysis (PCA), using the singular value decomposition method. Second, we used Hierarchical Clustering of Principal Components (HCPC) based on Ward's method of agglomeration and Euclidean distance on our standardized dataset that contains 32 stations and 21 variables (i.e. XRD and XRF dataset). All analyses were

conducted with the R statistical software v.4.3 (R Core Team, 2018) with the following packages: FactoMineR (Lê et al., 2008), factoextra (Kassambara and Mundt, 2016), FactoInvestigate (Thuleau and Husson, 2020), corrplot (Wei & Simko, 2017), Factoshiny (Vaissie et al., 2017), PerformanceAnalytics (Peterson et al., 2014), and tidyverse (Wickham et al., 2019).

3 Results

Beginning with the larger scale of geological observations, the results will describe our findings in a sequence of GPR profiles, grain size distributions, mineralogical and elemental compositions, and multivariate statistical analysis.

3.1 Geomorphology of Merapi Sedimentary Systems

Reworked volcaniclastics from Merapi eruptions are transported by Opak River and deposited in channel-side bars during the proximal stage, followed by point bars on medial, and a mid-channel bar before eventually accumulate as estuary deposits in the distal part (Fig. 4). The shifting of Opak River trajectory from SE to SW during the medial stage is influenced by the presence of Opak Fault, where the river follows the normal fault's axis (Fig. 1A). Slope angle also affects Opak River's depositional environment (Fig. 4B) which shows a contrast between (1) proximal – medial steep slope angle (8.27°, 14.54%, bearing N 169.5° E) and a gentler slope of (2) medial – distal (0.32°, 0.52%, bearing N 219° E). A mid-channel bar is present in the distal site of Opak River, 5 km NE of the Opak Estuary (Fig. 5A). The mid-channel bar is non-migrating and elongated, parallel to the flow of Opak River. Trenching in the mid-channel bar shows a planar cross-bedding with stratified gravels embedded in the foresets (Fig. 5C) on the lower part of the trench. In contrast, the upper part shows a good sorting, finer planar cross-stratification overlain by the imbrication of crudely-bedded gravel (Fig. 5B). Subsequently, the distal part is also the site of Opak Estuary. According to its geomorphologic classification (Perillo, 1995), Opak Estuary is a river-dominated estuary with tidal river influence since the saltwater front is not well-defined, unlike delta-front estuaries (Fig. 2A). The tidal range in Opak Estuary and Parangkusumo Shoreface is categorized as micro-tidal (Masselink and Short, 1993). The NE-SW motion of Opak River's discharge creates a tidal inlet (Fig. 2B) within the washover barrier sand (Fig. 2C). Parabolic sand dunes are present approximately 3 km southeast of Opak Estuary. The NE wind flow pattern coming from the south creates a shallow, dish-shaped depression at the stoss side of these parabolic dunes, further classified as a saucer-type blowout surface (Hesp, 2002).

3.2 GPR Profiles

GPR profiles across the Parangkusumo shoreface and the parabolic sand dune show distinctive reflection patterns with several geometries and intensities (Fig. 3). An illustration of the parabolic dune transect is shown by Fig. 3A-i. GPR line B begins at the blowout surface and moves upwind to the lee with a SE-NW direction. The section reveals an internal geometry of the parabolic sand dune with different angularity of cross-strata and interdune surfaces (Fig. 3B).

The modern surface slope angle from the stoss side to the top of crestline is 4.5° while the lee side to top of crestline reached 32.5°. Cross-strata surface and interdune surface reflection patterns are visible down to approximately 15 m effective depth from the surface of this dune. An interpreted established foredune is visible roughly 6 m beneath the modern lee surface with a steeper stoss-side slope of 13° and lee-side slope of 42° compared with the modern dune surface.

GPR line C with 90m length from the foreshore towards the backshore passed a substantial 4 m elevation height difference on the berm (Fig. 3C). The effective depth of this GPR line reached approximately 6 m below the surface, shallower than the parabolic dune GPR line. A comparison between the uninterpreted and interpreted section is presented within the inset of GPR line C (Fig. 3C-i and 3C-ii), revealing upslope climbing clinoforms (red vector arrow) with angle of repose inclining towards NW, unidirectional with the swash motion of waves coming from Indian Ocean.

3.3 Grain Size Distribution

Grain size distribution is plotted against the distance from source to sink and the depositional environment (Fig. 6). The proximal site has the average coarsest grains of all sites, with 24-40% of its grain size fraction consisting of very coarse and medium sand combined. The pre-fault sediment of S6A has 44% of its grain size fraction made of very coarse sand, while the post-fault sediments are 28-48% medium-sized sand. The distal part of Opak River follows post-fault medial sand trend, having 28-44% of its grain size faction in medium-sized sand. The northward interface of Opak Estuary adjacent to the river has 36-48% average grains consisting of medium sand, however, the southward interface adjacent to the Indian Ocean has 28% of its average grain size consisting of medium to fine sand. Sample S12A, a surface deposit on top of the estuary, has the coarsest grain of all samples collected from source to sink, with an average of 60% of its grain size fraction consisting of very coarse sand. A gradual trend of average grain size variability occurs in the Parangkusumo shoreface samples, where the foreshore has an average of 48% medium sand, and two backshore samples are consisting of 64% fine sand and 44% very fine sand. The aeolian deposits are consisting of medium sand with an average of 40-56% of their grain size fractions across the blow-out surface, stoss, and lee. It is worth to note that despite sharing a similar average grain size across the bedforms, the aeolian samples have a linear decreasing trend of very coarse-to-coarse and very fine-to-silt sized grains parallel to the direction of prevailing wind, whereas their medium-sized grains are gradually increasing.

3.4 Geochemical and Multivariate Statistical Analysis

Five main minerals are identified in the Merapi sediments based on their signature peak patterns from XRD analysis (Fig. 7A), which include anorthite ($CaAl_2Si_2O_8$), albite ($Na(Si_3Al)O_8$), augite ($Ca(Fe,Mg)Si_2O_6$), enstatite ($(Mg,Fe)SiO_3$), and calcite ($CaCO_3$). The quantification of bulk mineralogical

composition is tabulated as averages for each sample (Table 2). A plot of mineralogical content with depositional distance (Fig. 7B) shows an uneven distribution from proximal to distal which appears to correlate to variations in grain size (Fig. 6). To provide clarity in discerning this relationship, we grouped the anorthite and albite as plagioclase feldspar (PF) and augite and enstatite as pyroxene (Px), similar to the Mars analog study in Iceland (Sara, 2017; Thorpe et al., 2019) and Gale Crater investigation (Rampe et al., 2020).

Despite plagioclase feldspar abundance over pyroxene is clearly visible from source to sink (Fig. 8), we observed variability in the sorting of these mineralogical compositions throughout the sedimentary systems by plotting a ratio of Px/PF against the depositional distance (Fig. 8), with host rock average Px/PF ratio of 0.43. We combined Px/PF ratio against depositional distance with average grain size function (Fig. 9A). In the proximal site, the dominant plagioclase feldspar sorting (Px/PF ratio of 0.31-0.38) consists of coarse-to-medium sand deposited in channel-side bars, whereas the medial is deposited in point bars. Sample S3A is marked as it is the only proximal sample inclined towards pyroxene sorting, despite retaining similar average grain size with the remaining proximal samples. The lowest Px/PF ratio (0.31) of all samples belongs to the point bar deposit of proximal-medial interface (S6A). The pre-fault medial site still follows the trend of plagioclase feldspar sorting from the proximal site, despite the depositional environment change from the channel-side bar to a point bar. The post-fault medial site shows a strong pyroxene sorting (Px/PF ratio of 0.45-0.70), entirely deposited in point bars, with average grain size function of medium-to-very fine sand. We marked sample S8A as it is the only post-fault medial sample inclined towards plagioclase feldspar sorting, while having the lowest average grain size (very fine sand) of all measured samples. The estuary samples are dominant in pyroxene sorting (Px/PF ratio of 0.47-0.63), and their average grain size function are between coarse-to-fine sand, which included the coarsest grain of all measured sample (S12A), a top surface deposit within the estuary's washover barrier sand (Fig. 2C). The shoreface sediments clearly distinguished foreshore sample from the backshore further passing the berm as foreshore sample has medium sand compared to backshores' fine-to-very fine sand despite having similar pyroxene sorting (Px/PF ratio of 0.53-0.60). In the wind-driven environment, aeolian process shows that sorting occurred both in mineralogical and average grain size function, as the Px/PF ratio variability is accompanied with lesser concentration of coarse sand and more concentration of medium sand upwind (Fig. 6). The pyroxene sorting trend is shifting (Px/PF ratio of 0.56 to 0.44) in the lee and stoss to plagioclase feldspar sorting in the blowout surface (Px/PF ratio of 0.42). This study's modern aeolian dune has an average value of Px/PF ratio of 0.47, whereas the modern aeolian on Mars' Bagnold and Namib Dune are between 0.55-0.75. The ancient aeolian units of Stimson formation have a Px/PF ratio are 0.29-0.70 (Fig. 9B).

Plot of major elemental (Al, Si, Ca, Fe) and minor elemental compositions (K, Mg, Mn, Na, P, S, Ti; Fig. 10A) are presented with distance and depositional environment. In addition, oxides are also identified through XRF analysis (Fig.

10B). The influence of Opak fault is clearly seen between samples S6A and S7A, where prior to the interface of the fault (S6A), Fe and Fe2O3 are increasing. However, post-fault S7A shows a major decrease in those elemental and oxide abundance. Sample S12B also distinguishes itself from the rest of the measured samples because of the most abundant Fe and Fe2O3.

A hierarchical clustering (Fig. 11A) of mineralogical components based on XRD and XRF data reveals three distinctive clusters. A PCA plot is shown to elaborate the clustering of the analyzed samples (Fig. 11B). Interpretation of this clustering is derived from bulk mineralogical and elemental plot against depositional distance (Fig. 7 and Fig. 10). A total of 93.99% variability resemblance shown by PC-1 has established 3 clusters each with its own distinction, in particular sample S12B is compared to the rest (Cluster 1, Fig. 11). This distinction is a result of sample S12B having the lowest albite (7.15%) and enstatite (7%) but highest anorthite (59.05%) from all measured samples, in addition to the sudden peak of minor elements (e.g. manganese, phosphorus, and titanium) across the study area. The second cluster (red color) is characterized by positive axis coordinate for PC-1 (Fig. 11B), sharing a narrow range of albite (22.5% - 28.9%) and anorthite (35.5% - 39%), has the highest amount of iron (S10A and S11B) and all are in distal part. The last cluster (grey color) has negative PC-1 axis value, characterized by a wide range of albite (24% - 48.35%) and anorthite (26.8% - 44.3%), distributed widely in proximal, medial, and distal areas.

Results from the CIA and A-CN-K ternary diagram (Fig. 12) show that Merapi volcaniclastics are categorized within a low chemical alteration, having an average of 45 CIA value, with sample S6A notably having the highest CIA value of 58. Average CIA value from Gale crater (Mangold et al., 2019) and Stimson formation (Bedford et al., 2020) samples show a cluster (pale grey shade) of CIA ~50-56 when overlain with Merapi volcaniclastic samples (pale red shade). Overall, the diagram shows a general agreement of weathering trend in decreasing CaO, increasing felsic minerals, and the samples are clustered within the range of plagioclase feldspar relative to K-feldspar.

4 Discussion

Results from our analysis of the Merapi fluvio-coastal-aeolian sedimentary system show that mineralogical sorting correlates with the depositional distance and the subsequent environments. We focused the discussion towards mineralogical, elemental, and spatial variability within each depositional environment on Merapi volcaniclastics. We then provide some insights on Mars sedimentary systems' hypotheses based on the findings of our study.

4.1 Merapi Volcaniclastics from Source to Sink

The parabolic dune formed along Parangkusumo coast is a product Merapi pyroclastics carried downstream by Opak River. The river formed Opak Estuary at its distal part, and longshore current transported the estuary's sediments to source Parangkusumo Shoreface's deposit through the motion of Indian Ocean

wave with its eastward energy flux vector (Ray et al., 2005). Shoreface sediments are transported by the prevailing NW wind from Indian Ocean, resulting in the formation of parabolic sand dunes with their arc tilting to NW.

In the proximal site, Opak River geomorphology is affected by the lahar-carved subsidiaries (Fig. 1). The variability of fluvial depositional subenvironments along the Opak River is influenced by the geomorphology of the river, where in the proximal part, the river retained a relatively more linear flow as a direct influence of the steep slope angle from Merapi. In the medial part, as the river runs along a much gentler slope, the trajectory of the river started to meander, thus providing the essential site for point bars to form. Further downsystem the river geomorphology is able to form mid-channel bar. In the distal part, the river is substantially wider (Table 1) and deeper than its proximal and medial counterpart, which provides an accommodation space for the non-migratory mid-channel bar to form. The trenching in this mid-channel bar (Fig.5) shows that variability in the vertical succession suggests a cyclic mechanism from different episodes of fluvial hydrodynamic flow. Gravel inclusions can be attributed to high energy in an upper flow regime due to downstream ebb accumulation which can transport heavier grain, whereas the fine planar cross-stratification is influenced by a lower flow regime.

The Parangkusumo Shoreface and the parabolic dune both shared similar mineralogical and elemental compositions, suggesting the dune is a product of aeolian transport from the same provenance. There might be an influence of Nglanggran Formation (Fig. 1A, Tmn) eroded materials within the dunes' composition, considering on the proximity of the outcrop to Opak River and Parangkusumo Shoreface. However, erosion from Nglanggran Formation is more likely derived from the faulting and transported downsystem by fluvial process, rather than directly from the wind itself, considering the NW prevailing wind direction from Indian Ocean. Therefore, we believed the materials introduced by Nglanggran Formation will be deposited subsequently in the estuary before they enter the shoreface environment, which eventually sourced the dune sands.

Shoreface GPR profile (Fig. 3C) provides shallower depth than the parabolic dune GPR profile (Fig. 3B) because saline water attenuates GPR signal. The parabolic dune GPR profile (Fig. 3B) suggests an initial dune formed as a base of topographical height which became a catchment for aeolian sediment accumulation. This may have eventually led into the development of a secondary dune, initiated by continuous aeolian processes and excluded from beach processes (Sloss et al., 2012a, 2012b).

Development of the parabolic dune over a period of time will form along axis oriented with the prevailing wind direction. The established foredune shown in the GPR section suggests an incipient foredune in the past which formed across an older blowout surface and reduced the flow of aeolian volcaniclastic sand coming from the shoreface (Carter et al., 1990; Hesp 1999). When the incipient foredune develops, sand inundation decreases while nutrient levels and vegetation cover increase, resulting in stable dunes and thus hindering further

migration. The lee slope became a fertile ground for shrub plant species to grow, which prefer more stable conditions (Hesp 1999, 2002). Sand is gradually deposited on the seaward slope, and sometimes the crest of the dune which slowly becomes larger forming an established foredune. Due to the development of a recent, more stable dune on modern surface, continued aeolian transport will likely cause an increase in dune height, and with it a higher threshold for the volcaniclastic sands, making it less likely to migrate the dune further inland.

4.2 Influence of Depositional Environments for Merapi Volcaniclastics

The grain size variability consists of decreasing particle size, starting from proximally very coarse-to-coarse grains deposited in channel-side bars, and the first point bar before it reaches the Opak Fault (Fig. 6). The interface between proximal to medial site of Opak River is essential as it provides the first evidence that mineral sorting occurs independent from the sedimentary bedforms. Despite having a different fluvial depositional subenvironment, the channel-side bar of S5A and point bar of S6A still retained plagioclase feldspar as its dominant mineral sorting preference. The preferential of mineral sorting in the proximal site is plagioclase feldspar, whereas the medial and distal part is pyroxene (Fig. 8), indicating plagioclase feldspar as the groundmass mineralogy in these systems and pyroxene as the phenocrysts, favorable to the findings from Preece et al. (2013). This could explain the pyroxene sorting "spike" in sample S3A (Fig. 8), which might be the accumulation of a locally-eroded and transported pyroxene from a more recent Merapi eruption.

In the medial site, Opak Fault alters the trajectory of the river from NE to SW and contributes to the most abundant silt-sized sediments in sample S8A (Fig. 6). This is influenced by an upthrown block of Opak normal fault in the east side of the river. The eastern bank of the river is also known as an exposure for Semilir Formation (Tmsc) outcrop (Fig. 1), consisting of an already finer material (tuff-breccia, pumice breccia, andesitic tuff) compared to the younger pyroclastic material from Merapi. The presence of weathered materials from Semilir Formation outcrop are shown within the interface of pre- and post Opak Fault in CIA and A-CN-K ternary diagram (Fig. 12), which explained the contrast of sample S6A CIA value compared to the rest of the sample. The exposure and erosion of Semilir Formation might influence the sample S8A as the only post-fault medial sample that has plagioclase sorting dominance instead of the pyroxene-dominant like the rest of the post-fault medial samples. The finer tuff-breccia material is also an indication to explain sample S8A as the sample with the lowest average grain size function across the sedimentary system (Fig. 9A).

In the distal site, the abundance of very coarse to coarse sand from source to sink is notably decreased once the sediments are transported inland in the shoreface, due to the presence of the berm. The change of primary sedimentary transportation from fluvial and longshore currents to aeolian processes is shown clearly in the plot (Fig. 6) where medium, fine, and very fine sand started to dominate sediment particles in the parabolic sand dune. Finer grains are more

efficiently transported further landward in the coastal aeolian system, leaving an accumulation of the coarser materials in the foreshore, also visible as an average grain size plot in the blowout surface of the dune (Fig. 6 and Fig. 9A). The trend of grain size variability and Px/PF ratio on the dune site can be attributed to the parabolic sand dune geomorphology where the saucer-type blowout surface acts as a catchment area for sediments carried out by the wind from backshore. The blowout surface gradually develops slope gradient in the stoss-side until it reaches a threshold at the tip of the crestline, where sediment particles are driven by additional force of gravity to move landward by settling in lee-ward side. Another notable result in this environment is the presence of a linear decreasing trend from medium, fine, very fine sand, and silt throughout blowout surface, stoss, and lee, which is parallel to the direction of prevailing wind (Fig. 2).

X-Ray Diffractometer by Aini et al. (2019) had shown Merapi's plagioclase to bear 44% anorthite and 54% albite. Atomic Absorption Spectroscopy (AAS) by Wahyuni et al. (2012) revealed Merapi's volcanic ash composition of SiO_2:Al_2O_3:CaO as 53:19:9 in distributive percentage, strengthening the calc-alkaline basalt-andesitic nature of Merapi volcaniclastics (Camus et al., 2000). Similarly, Wahyuni et al. (2012) included Inductively Coupled Plasma Mass Spectrometry (ICP-MS) to determine the minor elemental composition of the volcanic ash. These two combined methodologies of AAS and ICP-MS had recorded major elemental compositions (Al, Si, Ca, and Fe) and minor elemental compositions (K, Mg, Mn, Na, P, S, and Ti) (Wahyuni et al., 2012). All of these detected mineralogical and elemental compositions are recorded in our study from source to sink, which shows that Merapi pyroclastics are transported actively along the sedimentary systems we investigated throughout.

The minor presence of calcite in Merapi pyroclastic was a subject of a precursor research by using an experiment using time-variable decarbonation based on Merapi basalt-andesite and Javanese limestone to unravel the presence of $CaCO_3$ in Merapi's magma (Deegan et al., 2010). It is possible that carbonate materials are present as a contaminant melt in xenoliths and Merapi feldspars (Deegan et al., 2010) thus their presence can be traced from the source towards the sink. The combined results from bulk mineralogical composition and HCPC – PCA plot with PC-1 value of 93.99% confirmed the sediment provenance comes from calc-alkaline, basalt-andesitic Merapi source rocks (Camus et al., 2000). The high abundance of plagioclase feldspar represented by albite and anorthite can be attributed to the dominant groundmass phase of the Merapi volcaniclastics whereas augite and enstatite as the phenocrysts from modern Merapi eruptives (Camus et al., 2000; Wahyuni et al., 2012; Preece et al., 2014).

Observation from our research suggests that mineral and sedimentary sorting that occurs throughout the entire sedimentary system is likely influenced not only by a single event (i.e., Merapi volcanism), but also from the depositional environments which the river flows and the complex interplay between estuary, shoreface, and backshore's aeolian activity. For example, ancient pyroclasts

from previous Merapi eruptions might get transported (i.e., as a suspended material or through bedload flux) downstream, deposited on a fluvial bar downsystem. Opak fault might excavate deeper sediments and continue to rework the sedimentary sorting processes. This is particularly observed with coarser grain-sized sediments compositionally enhanced from Opak fault to right before the Opak Estuary, while no trend is observed before the fault. Additional sources can also influence sand dunes and samples from the coast, as materials are directly coming from the sea, presumably transporting pyroclastics from various volcanic sources (i.e., other Merapi tributaries or other volcanoes northward of Merapi). NW winds from Indian Ocean carried suspended materials not only from the local shoreface and Opak Estuary, but along the entire shoreface which encompasses another estuary from neighboring Progo River. This river is another drainage that flows from dendritic sources at the feet of Merapi Stratovolcano, with its anterior located 9 km NW of Opak River, also transporting Merapi volcaniclastics downstream (Fig. 1), possibly enriching elemental abundance of the aeolian deposits further windward.

4.3 Significance of Studying Mars-like Sedimentary Systems on Earth

Addressing martian hypotheses on Earth with a terrestrial analog study is beneficial since the samples can be collected primarily by in-situ fieldwork. This has been proven from previous research such as mineralogical identification from field observation and laboratory analysis in Ka'u Desert, Hawaii (Seelos et al., 2010) which established an analogous young basaltic materials from ancient lava flows on Earth and Mars. Dyngjusandur sand deposit (Iceland) is considered analogous because basaltic minerals along with plagioclase feldspars and pyroxenes resembled Mars' crustal composition found in Gale crater's Stimson formation (Sara, 2017). Previous Mars studies have focused on solely basaltic environments, however, missions in Gale crater (McSween Jr. et al., 2009; Schmidt et al., 2014; Sautter et al., 2015; Sautter et al., 2016; Treiman et al., 2016; Siebach et al., 2017; Bedford et al., 2019) shows that martian crust is more geochemically diverse with some locations containing pyroclastic deposits such as Home Plate, Gusev crater (Squyres et al., 2007). The Mars Exploration Rover, Spirit, encountered possible pyroclastic deposits on the NW flank of Husband Hill, on the Cumberland Ridge, and on Home Plate (Squyres et al., 2006; 2007). The deposits on Husband Hill and Cumberland ridge are part of the Wishstone class rocks which were investigated using the APXS (Alpha Particle X-Ray Spectrometer) instrument on the Spirit rover and were found to have a unique chemistry with a higher Al/Si ratio than any other rock type in Colombia Hills. This geochemistry was indicative of a high abundance of plagioclase with some pyroxene and olivine, and minor amounts of Fe oxides and oxyhydroxides (Squyres et al., 2006). Wishstone class rocks also contain poorly sorted mm-scale clasts within a fine matrix which include angular clasts indicative of either explosive volcanism in a pyroclastic eruption, or impact processes (Squyres et al., 2006). Evidence for pyroclastic deposits on Home Plate included bomb sags, rounded grains that were similar in appearance to accretionary lapilli, and an infrared spectra that suggested a high abundance (45 wt%) of basaltic glass (Squyres et

al., 2007). The Home Plate deposits have an alkali basalt geochemistry suggesting that they may have formed through a phreatic eruption of alkali basalt lava (Squyres et al., 2007). Orbital evidence for pyroclastic deposits on Mars has also been found at the Medusa Fossae Formation which is a large, friable, eroded tephra deposit (Scott & Tanaka, 1986; Greeley & Guest, 1987; Bradley et al., 2002), and at the Cerberus Fossae fissure system in Elysium Planitia which is a low-albedo, high-calcium pyroxene-rich unit (Horvath et al., 2021).

Our research aims not to compare an already established Mars analog such as Iceland and Hawaii with Merapi, but to give additional insights on Mars sedimentary systems based on our findings. The basaltic nature of Iceland's and Hawaii's magmatic composition is different from the Merapi's basaltic to basalt-andesitic magma. However, is it possible for Mars during its past to have volcanoes with a similar magmatic composition like Merapi? We might not be able to fully understand the provenance of this reworked igneous material today on Mars; however, we can see the deposits of basaltic to andesitic minerals on Gale crater (McSween Jr. et al., 2009; Schmidt et al., 2014; Treiman et al., 2016; Siebach et al., 2017; Bedford et al., 2019) and reworked pyroclastics on Home Plate, Gusev crater (Squyres et al., 2007). Indeed, magmatic and mineralogical fractionation are active scientific frontiers on Mars geology. In Gale crater, Curiosity rover has delivered over 30 drilled samples of sedimentary material into its XRD instrument, CheMin, and found abundant plagioclase feldspar and pyroxene minerals, in addition to evolved igneous minerals such as sanidine, tridymite, and cristobalite that are present at certain locations along its traverse indicative that basalt is not the only sediment source (Vaniman et al., 2014; Treiman et al., 2016; Morris et al., 2016; Rampe et al., 2020). Our data from the Merapi sedimentary systems show a high abundance of feldspar and pyroxene, and understanding how these minerals are sorted relative to each other as they are transported in different sedimentary systems will aid in the interpretation of sediment source and transportation on Mars.

4.4 Insights for Mars Sedimentary Systems Impacted by Pyroclastic Materials

The proximal environment of Merapi is home to more significant pyroclastic ejecta such as block and bomb. The recorded sedimentary texture of lower unit in Home Plate exhibits clast (referred to as bomb sag, Squyres et al., 2007) as inclusion within a parallel stratification, whereas the upper unit shows cross-stratification made of fine-grained and well-sorted materials. The bomb-sag is also present in the proximal area of Merapi, suggesting the Home Plate in Gusev Crater is located in either the vicinity of proximal volcanism, or to an extent of proximal to medial interface. It is common to see the bomb inclusion on the proximal area covered with pyroclastic sedimentary unit in Merapi (Fig. 13). The reworked materials in Home Plate shows the presence of albite, anorthite, and pyroxene from Alpha Particle X-ray Spectrometer (APXS) and CIPW normalization (Squyres et al., 2007), which are also identified in our samples from Merapi using XRD.

One notable way that explosive volcanism can impact sedimentary systems is through the incision of gullies on Merapi's surface from lahar flows which directs the initial trajectory of the Opak river tributaries, impacting the direction of any pyroclastic flows. Eruption of lava on martian volcanoes have been reported to initiate valleys on Mars (Gulick and Baker, 1990), such as Alba Patera and Apollinaris Patera (Alemanno, 2018). In Merapi volcaniclastic sedimentary systems, our results show that explosive volcanism affect the sedimentary from source to sink as various fluvial depositional subenvironments are formed with definitive distance, (e.g. the channel- side bars in the proximal site, point bars in the medial, and mid-channel bar in the distal part of the river). This suggests that on these volcanoes where similar eruptives have occurred, similar sedimentary deposits could form on the sides of these volcanoes provided sufficient water existed at the surface to support a river system. If pyroxene dominates the phenocryst mineralogy in these systems and feldspar dominates the groundmass, similar to what we see in Merapi, then we would expect to see the preferential sorting of feldspar in proximal units relative to pyroxene, and pyroxene over feldspar in medial-to-distal setting.

Volcanic eruption and aeolian processes impact the formation, migration, and evolution of volcaniclastic dunes (Edgett and Lancaster, 1993; Hooper et al., 2012; Grotzinger et al., 2014). The Parangkusumo coastal sand dune is a product of complex interaction between volcanic eruption and fluvio-coastal-aeolian sedimentary systems. The interplay between these sedimentary systems eventually provides the sediments' provenance for creating the parabolic sand dunes. Numerous studies of the martian surface had shown the volcaniclastic dunes on Mars (Greeley et al., 1992; Grotzinger et al., 2005; Schmidt et al., 2014; Lapotre and Rampe, 2018; Payré et al., 2020), their mobility (Bridges et al., 2012) and the presence of ancient fluvial channels (Carr, 2012) could be linked with transported volcaniclastics by the fluvial system on Mars in the past. A terrestrial analogous study at Sunset Crater, Arizona (Hooper et al., 2012) had described a challenge of the missing step in sedimentary transportation from the provenance to the aeolian system, and the involvement of possible fluvial processes that deposit these sediments. Our research shows that reworked igneous materials from fluvial sedimentation significantly aids in the incorporation of volcaniclastic materials from the source into distal aeolian deposits, as it is observed by the mineralogical and elemental similarity drawn from our multivariate statistical analysis with 93.99% PC-1 value. It implies that any pyroclastic ejectas from Merapi are transported further downsystem by Opak River from proximal, medial, and distal part, before eventually deposited in the shoreface and carried landward with the introduction of aeolian processes. In Gale crater, it has been hypothesized that the recycling of ancient fluvial deposits was an important contributor to aeolian sediments in the past (Bedford et al., 2020; Edgett et al., 2020). Our results support that fluvial deposits can contribute significantly to aeolian deposits in volcanic environments by transporting the reworked volcaniclastics of along the fluvial trajectory, and the interface between fluvial-aeolian sedimentary systems will become the site of aeolian deposits' provenance, as

seen by the interaction between Opak River – Opak Estuary – Parangkusumo Shoreface.

Whether or not the Northern lowlands of Mars held one or more oceans in the past is a hotly debated topic (e.g., Head et al., 1999; Malin and Edgett, 1999; Clifford and Parker, 2001; Carr and Head, 2003; Ghatan and Zimbelman, 2006). Horizontal terraces at the edges of the volcanic Northern plains have been interpreted as paleoshorelines, representing an ancient contact between land and the paleo-ocean (Head et al., 1999; Clifford and Parker, 2001). These contacts were visible from an orbiter since the geomorphological expression is distinctive from its surroundings with a topographically inverted terrain (Head et al., 1999; Clifford and Parker, 2001; Di Achille and Hynek, 2010; Hughes et al., 2019). Although the establishment of paleo-ocean hypothesis in the Northern lowlands of Mars is more viable through paleo-climate reconstruction, if such an ocean did exist on Mars in the past, results from this research suggests that the distal part of fluvial discharge into a large standing water body would result in the build-up of a coarse, sedimentary material, such as what is seen at the geomorphological expression of the volcaniclastic shoreface in Parangkusumo coastline. This requires additional exploration on Mars to justify, especially at the edge of Northern lowlands. If the sedimentary structure or stratigraphic features can be imaged on those locations by means of physical extraction (coring, trenching) or non-destructive geophysical approach (such as GPR), there might be a clue to discern about the nature of Martian volcaniclastic paleo-coastline.

4.5 Implications for Mineral Sorting on Mars

Mars Odyssey Orbiter successfully mapped the crustal elemental composition of Mars, with a result of mineral assemblages ranging between basalt to basalt-andesitic origin (McSween Jr. et al., 2009). The first rock formation analyzed by Curiosity Rover was in Gale crater, performed by rover's instrument of Alpha Particle X-Ray Spectrometer (APXS) and ChemCam with a result of basaltic igneous origin (Schmidt et al., 2014). CheMin XRD from Curiosity Rover's instrument had identified mineralogical assemblages in the Windjana drilled sample of the Kimberley formation, Gale Crater (Treiman et al., 2016) composed of sanidine (21%), augite (20%), amorphous (15%), magnetite (12%), smectite (10%), and a possible detection of enstatite (marked with det? in Table 2 from Treiman et al., 2016). Bradbury group consists of fluvial conglomerate, sandstone and lacustrine mudstone units (Grotzinger et al., 2014; 2015). Geochemical analyses by the Curiosity rover's APXS and ChemCam instruments of the Bradbury group showed that it contains a diverse geochemistry indicative of input from subalkaline basalt at the Yellowknife Bay locality, trachybasalt in the Darwin outcrop, and a trachytic source in the traverse from Darwin to the Kimberley formation (Schmidt et al., 2014; Anderson et al., 2015; Le Deit et al., 2016; Siebach et al., 2017; Bedford et al., 2019). Further along the rover's traverse in the foothills of Mt Sharp, Curiosity encountered the Murray formation which consisted of predominately lacustrine mudstone (Grotzinger et al., 2015). Geochemical data from the Murray formation shows further evidence for

different sediment source regions that include a more silica-rich basalt such as a basalt-andesite with a SiO_2 concentration of 53.1 +/- 1.9 wt% (Bedford et al., 2019), and a possible rhyolite source at the Marias Pass locality (Morris et al., 2016; Bedford et al., 2019; Czarnecki et al., 2020). These evolved igneous assemblages are supported by mineralogical data provided by the CheMin XRD instrument which in particular showed high abundances of tridymite, a high temperature silica polymorph, present at the Marias Pass locality (Morris et al., 2016).

Our results favor the interpretation of incongruent dissolution for plagioclase feldspar found within the Murray formation, Gale Crater (Mangold et al., 2019). Drilled samples in Murray formation are dominated with plagioclase feldspar, and there has been discussion regarding alteration versus provenance effects for the ChemCam-derived interpretation of the drilling samples. Our study reveals that plagioclase feldspar is the most abundant mineral from source to sink, thus makes it possible to revisit the hypothesis of partial dissolution of plagioclase in Murray formation. It is believed that partial dissolution from plagioclase should be coupled with an observation of decreased in sodium (Mangold et al., 2019). This is consistent with our result from XRD and XRF, where decreasing abundance of plagioclase feldspar represented in proximal sample S2A and S3A (Fig. 7B and Fig. 8) is followed with decreasing amount of Na (Fig. 10A). The fluvially-transported S2A and S3A makes it possible to assume that alteration occured based on aqueous process.

Furthermore, we find pyroxene in a higher abundance relative to feldspar in medial and distal sites, deposited in point bars, mid-channel bar, estuary, shoreface, and the lee and stoss of the parabolic sand dune. The pyroxene sorting from Merapi is found on an average grain size from coarse-to-fine sand. Evidently, the pyroxene sorting occurs in the gentler slope of Opak River, where the river started to lose the gravity-driven potential energy which is derived from the proximal's steep-sloped angle. This suggests that fluvial sedimentary system is capable to transport pyroxenes further into the distal site as opposed to plagioclase feldspar, despite pyroxenes having higher density than plagioclase feldspar. This finding favors the hypothesis of fluvial sediment as the source sediment for Stimson formation (Bedford et al., 2020). Another notable result from our study is the variability of Px/PF ratio across the blowout surface, stoss, and lee that is similar with the findings of CheMin measurement from barchanoidal dune (Bagnold and Namib Dune) (Rampe et al., 2020). Our study shows that the upwind part (stoss) of Parangkusumo parabolic sand dune has less plagioclase feldspar concentration compared to the blowout surface of the dune, and become a site of a relatively higher density mineral (pyroxene) to accumulate. This is consistent with the CheMin findings of Gobabeb and Ogunquit Beach samples (Fig. 9B), where the upwind margin has less concentration of plagioclase feldspar compared to the downwind margin (Rampe et al., 2020).

5 Conclusion

Merapi volcaniclastics are a product of an active volcano that could provide in-

sights to constrain martian older and more recent volcaniclastics by focusing on unaltered anorthite, albite, and pyroxenes found on martian crust. We conclude that:

1. Quantification of mineralogical and elemental composition analysis from volcaniclastic stream sediment samples had shown a generally decreasing trend from source to sink, however, when an additional process of aeolian activity is introduced in the backshore environment, the elemental abundance is increased.
2. The grain size and mineral sorting exhibit a distinctive signature for each depositional environment from source to sink. This grain size and mineral sorting can be applied to constrain several Mars hypotheses, especially to address the geological diversity of Mars rover landing sites.
3. The result from multivariate statistical analysis shows a promising insight as a method of its own to establish provenance study, showing a favorable result with cluster analysis-based provenance studies in Gale crater.
4. The interconnected surface processes of volcanic cyclic eruption, fluvial discharge, longshore current, and coastal volcaniclastic aeolian sand dunes are all inseparable from shaping the geomorphology of a reworked volcaniclastic terrain in Merapi sedimentary systems.
5. Fluvial sedimentary system is capable to transport pyroxenes further into the distal site, despite pyroxenes having higher density than plagioclase feldspar.
6. Sediment recharge from Opak Fault shows pyroxene enrichment, and pyroxene sorting occurs from medial to distal, of which the river trajectory follows Opak Fault axis.
7. Wind-driven sorting in aeolian environment shows both mineralogical and average grain size function are gradually changing across the bedforms, parallel to the direction of prevailing wind, despite having similar average grain size.
8. Mineral sorting variability can be observed in bedforms regardless of its grain size distribution and the depositional environment of its sedimentary system. It is exhibited by 3 examples; (1) The proximal-medial interface of Opak River; (2) Shoreface samples retained dominant pyroxene sorting across the foreshore and backshore, however, the berm that separates the two bedforms is able to sort different average grain size from medium sand in the foreshore and fine-to-very fine sand in the backshore; (3) The parabolic dune samples (blowout surface, stoss, and lee) are all on average have medium-sized grains, however, the blowout surface contains more plagioclase feldspar compared to the pyroxene-dominant stoss and lee.

Acknowledgements

We are grateful for College of Petroleum Engineering and Geosciences (CPG) at KFUPM for funding our research and our expedition team in Indonesia. We would like to extend our gratitude to Prof. Jean-Philippe Avouac (California Institute of Technology), Dr. Elizabeth Rampe (Astromaterials Research and Exploration Science, NASA Johnson Space Center), and Dr. Ryan Ewing (Texas A&M) for the extensive discussion which helped the improvement of initial manuscript. We would also like to thank Mr. Firdaus Sigma and Mr. Nur Arasyi for helping us to acquire the stream sediment samples, along with Mr. Rahmaan Alam for GPR field data acquisition and pre-processing.

Tables

Table 1. Sample Identifications

Sample ID	Elevation (m)	Stream width (m)	Remarks
Stream sediment samples			
S2A	812	2	Channel-side bar
S3A	610	8	Channel-side bar
S4A	409	12	Channel-side bar
S5A	293	15	Channel-side bar
S6A	178	24	Point bar
S7A	124	26	Point bar
S8A	86	45	Point bar
S9A	48	50	Point bar
S10A	16	300	Mid-channel bar, NE tip
S10D	15	300	Mid-channel bar, SW tip, trenched and
S11A	1	-	Estuary, washover barrier sand, facing t
S11B	2	-	Estuary, washover barrier sand, facing t
S12A	2	-	Estuary, washover barrier sand, facing t
S12B	1	-	Estuary, washover barrier sand, facing t
Hand specimen samples			
S1A	1178	-	Dark grey mafic scoria
S1B	1167	-	Dark grey mafic diabase
S2C	812	-	Light grey intermediate porphyritic and
Shoreface samples			
C1A	1	-	Foreshore
C1B	2	-	Backshore
C1C	2	-	Backshore
Sand dune samples			
B1C	4	-	Lee side (slipface)
B1D	5	-	Stoss side (windward)
B1E	4	-	Blowout surface

Table 2. Identified Bulk Mineralogical Composition Based on XRD Spectra

Sample ID	Albite (%)	Anorthite (%)	Augite (%)	Enstatite (%)	Calcite (%)
Hand specimen samples					
S1A	32.45	36.05	12.7	17.7	1
S1B	32.6	35.9	12.7	17.8	1
S2C	36.25	34.65	12.85	15.4	0.85
Stream sediment samples					
S2A	41.2	31.1	9.15	17.15	1.45
S3A	30.35	29.45	24.75	14.8	0.6
S4A	40.1	31.65	10.85	16.65	0.85
S5A	48.35	26.8	4.6	19.45	0.75
S6A	31.05	44.3	9.45	13.8	1.4
S7A	38.5	29.75	13.55	17.15	1
S8A	39.6	31.55	10.75	17.15	1
S9A	24	33.8	12.5	28.15	1.6
S10A	28.9	38.8	13.35	16.9	2.1
S10D	27.1	36.15	16.7	19.05	1.05
S11A	32.2	35.35	16.7	15.05	0.75
S11B	22.5	39	28.6	9	0.9
S12A	33.2	28.9	22.6	14.6	0.75
S12B	7.15	59.05	26.35	7	0.4
Shoreface samples					
C1A	26.85	37.55	15.7	18.75	1.1
C1B	23.4	38.9	26.35	11.3	0.05
C1C	24.7	37.6	22.35	14.95	0.5
Sand dune samples					
B1C	28.35	35.5	23.65	12.1	0.45
B1D	32.9	36.05	16.05	14.35	0.7
B1E	34.8	35.25	15.95	13.5	0.5
Total Bulk Average	31.15	35.79	16.44	15.77	0.86

Figures

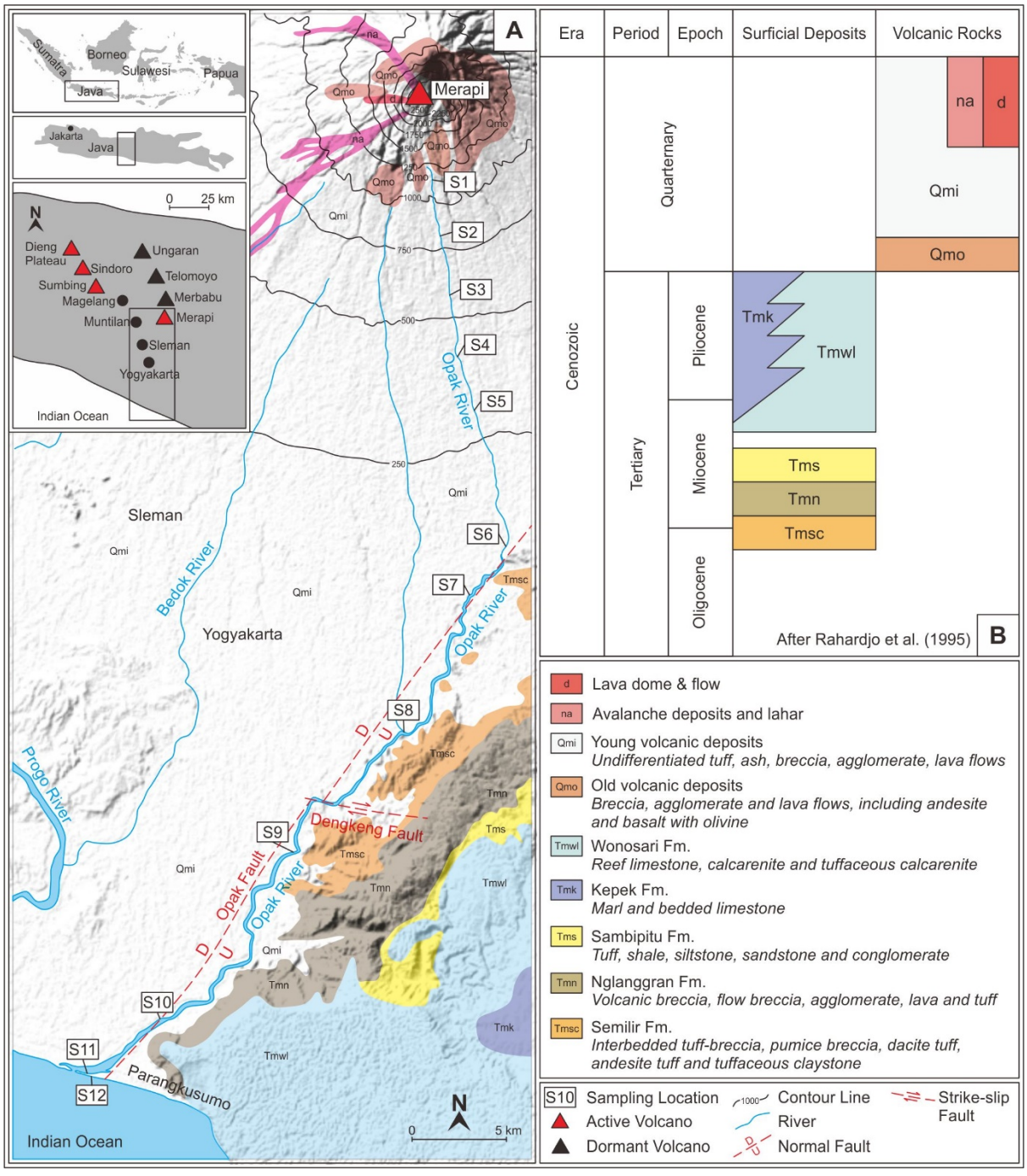

Figure 1. Geologic map featuring sampling locations from source to sink environments of Merapi – Opak River (Fig. 1A). Lithological units are based on

Rahardjo et al. (1995) (Fig. 1B). Notice the latest deposition of young volcanic deposits (*Qmi*) overlying older volcanic deposits (*Qmo*) and tertiary sediments. The lava dome and avalanche deposits (*d* and *na*) are present *in-situ* only on the proximal area of Merapi volcano.

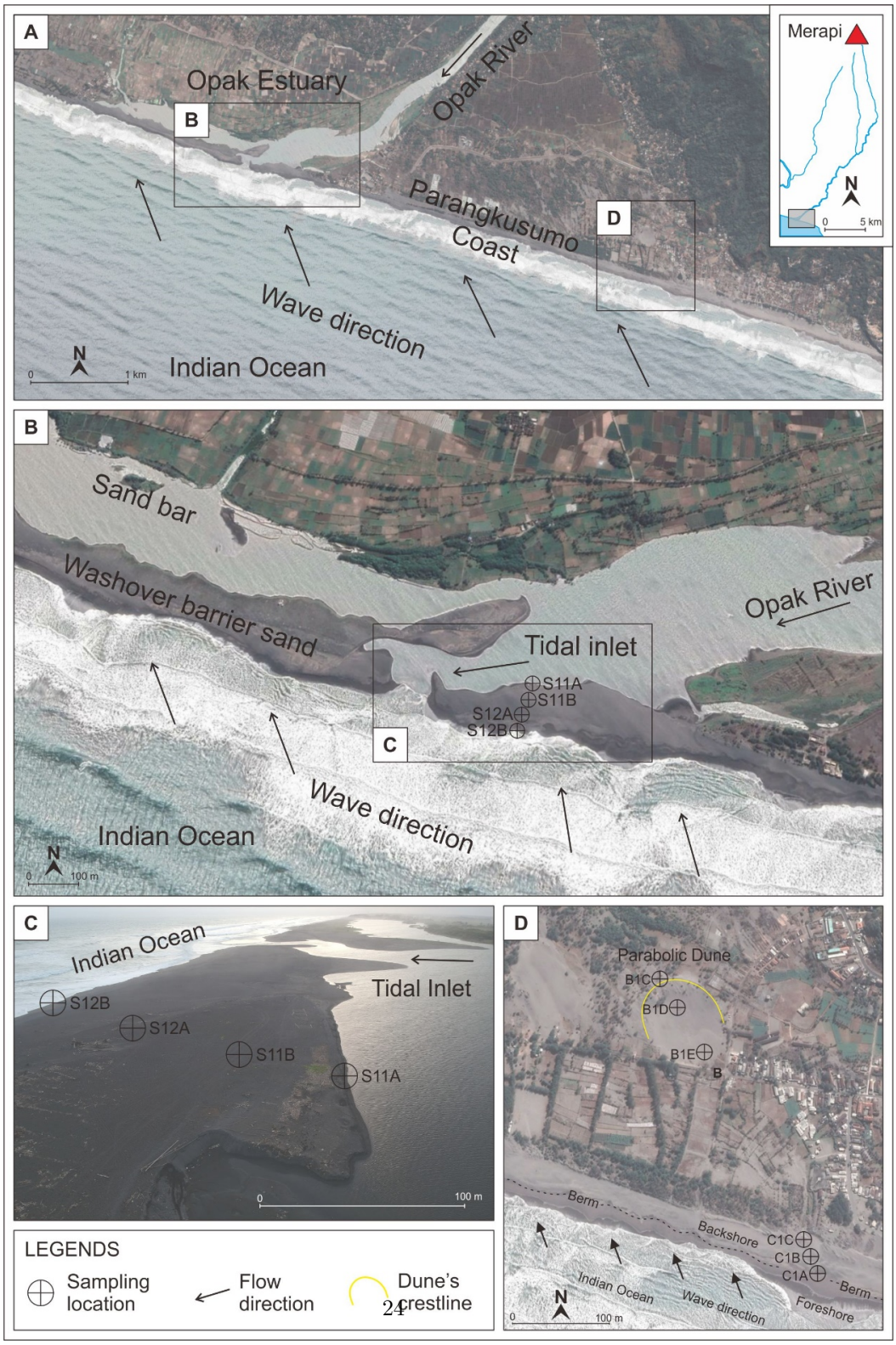
A
Opak Estuary
B
Opak River
Parangkusumo
Coast
D
Wave direction
Indian Ocean
N
0
1 km
Merapi
N
0
5 km
B
Sand bar
Washover barrier sand
Opak River
Tidal inlet
S11A
S11B
S12A
S12B
C
Wave direction
Indian Ocean
N
0
100 m
C
Indian Ocean
Tidal Inlet
S12B
S12A
S11B
S11A
0
100 m
D
Parabolic Dune
B1C
B1D
B1E
B
Berm
Backshore
C1C
C1B
C1A
Berm
Indian Ocean
Wave direction
Foreshore
N
0
100 m
LEGENDS
Sampling location
Flow direction
Dune's crestline

Figure 2. Distal part of this research showing Opak River, Opak Estuary, and the adjacent Parangkusumo Shoreface (Fig. 2A). Notice the bidirectional flow represented on the surface water between the river, estuary, and the ocean (Fig. 2B), interaction between tidal inlet and Indian Ocean (Fig. 2C) and the coastal parabolic sand dunes (Fig.2D).

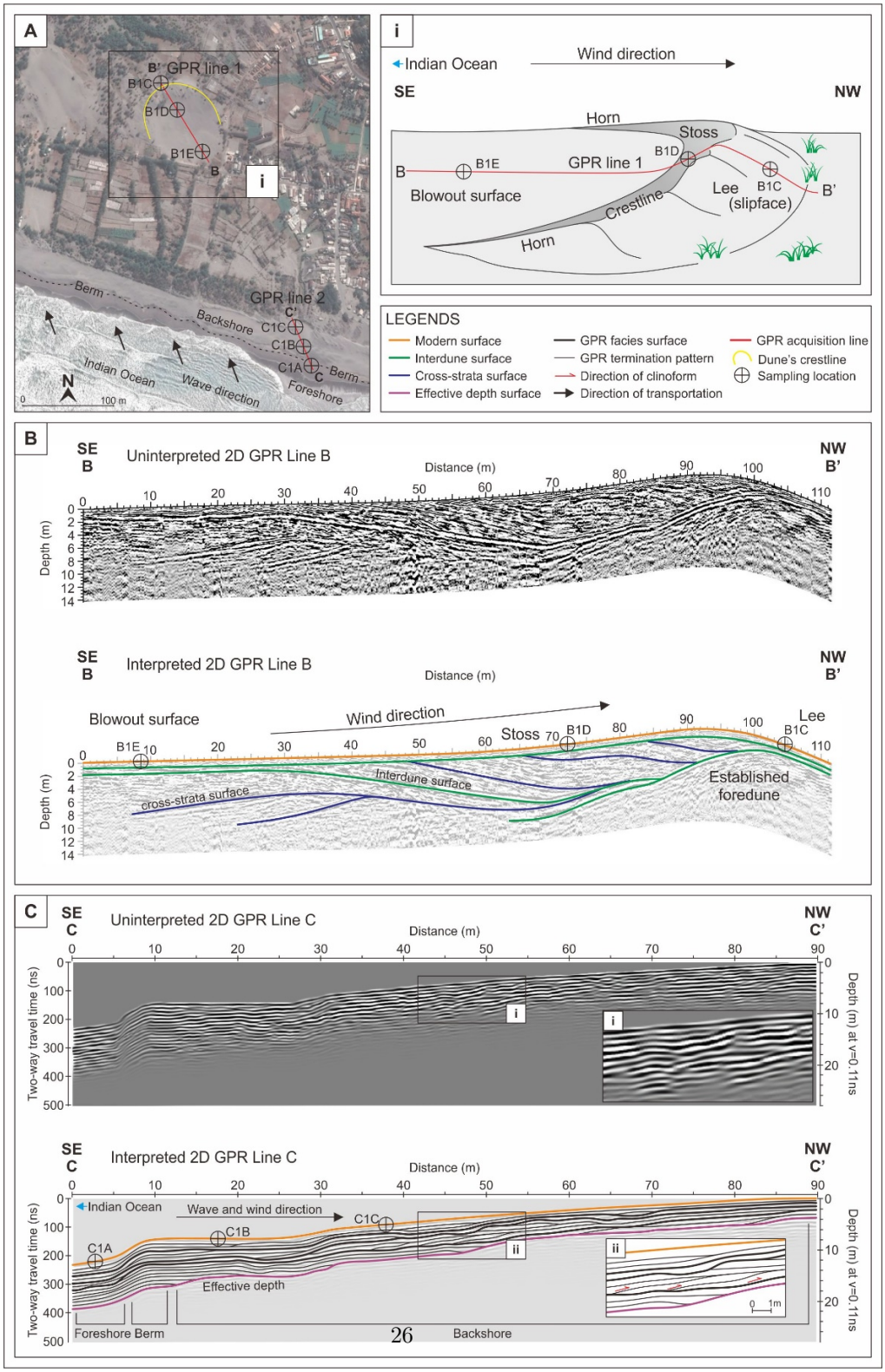
A
B' GPR line 1
B1C
B1D
B1E
B
i
Berm
GPR line 2
C'
Backshore
C1C
C1B
C1A
C
Berm
Foreshore
Indian Ocean
Wave direction
N
0
100 m
i
Indian Ocean
Wind direction
SE
NW
Horn
Stoss
B1D
B
B1E
GPR line 1
Blowout surface
Crestline
Lee
(slipface)
B1C
B'
Horn
LEGENDS
Modern surface
Interdune surface
Cross-strata surface
Effective depth surface
GPR facies surface
GPR termination pattern
Direction of clinoform
Direction of transportation
GPR acquisition line
Dune's crestline
Sampling location
B
SE
B
Uninterpreted 2D GPR Line B
NW
B'
Distance (m)
Depth (m)
SE
B
Interpreted 2D GPR Line B
NW
B'
Distance (m)
Blowout surface
Wind direction
Stoss
B1E
B1D
B1C
Lee
Interdune surface
cross-strata surface
Established
foredune
Depth (m)
C
SE
C
Uninterpreted 2D GPR Line C
NW
C'
Distance (m)
Two-way travel time (ns)
Depth (m) at v=0.11ns
i
SE
C
Interpreted 2D GPR Line C
NW
C'
Distance (m)
Indian Ocean
Wave and wind direction
C1C
C1B
C1A
ii
Effective depth
Foreshore Berm
Backshore
0
1m
Two-way travel time (ns)
Depth (m) at v=0.11ns

Figure 3. GPR acquisition profiles (Fig. 3A) and the illustration of dune morphology (Fig. 3A-i). Uninterpreted and interpreted GPR profiles are presented for each line (Fig. 3B and 3C). Notice the upslope climbing clinoforms (Fig. 3C-i and 3C-ii) formed within the shoreface profile as an indication of wave influence.

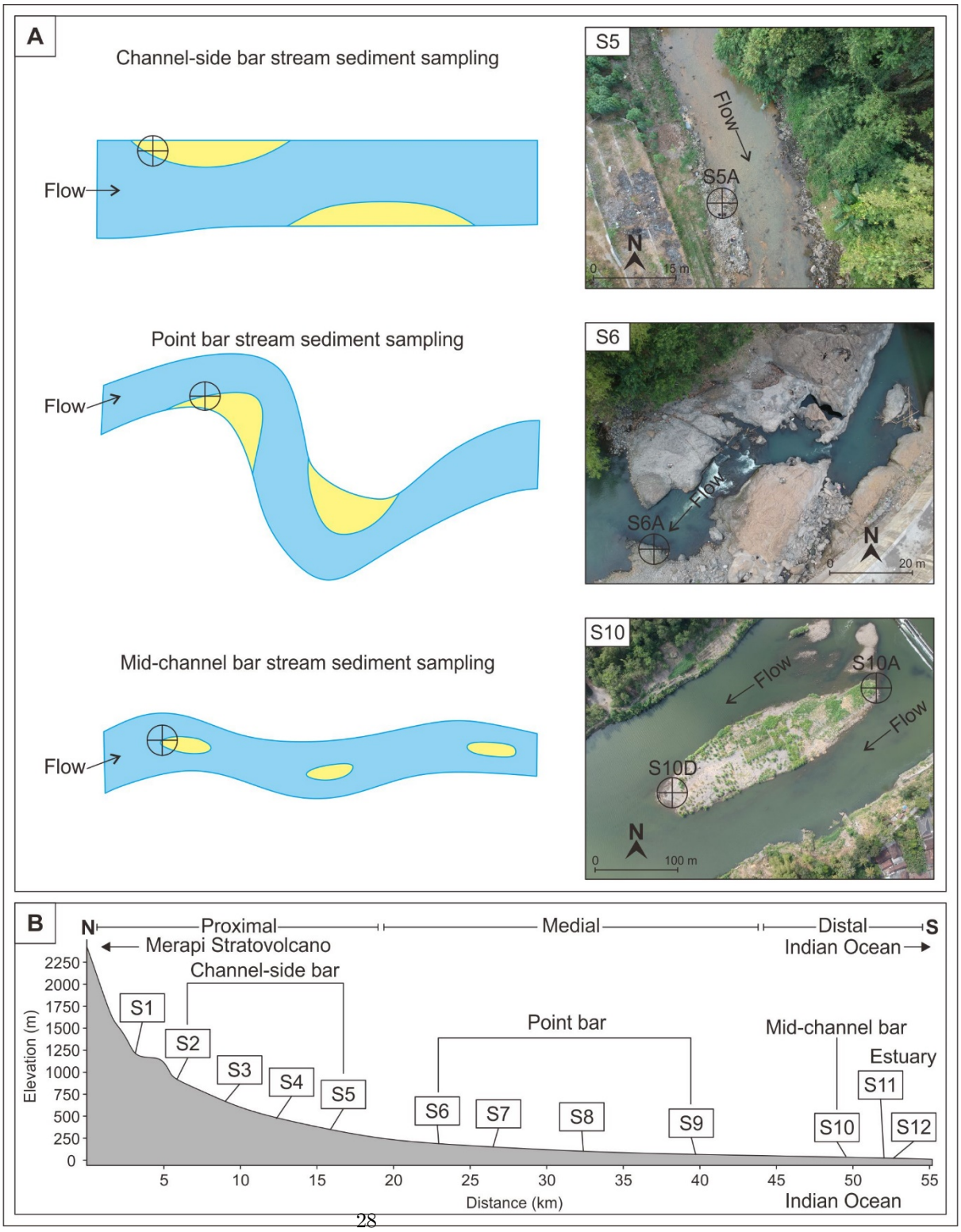
A
Channel-side bar stream sediment sampling
Flow
S5
Flow
S5A
N
0
15 m
Point bar stream sediment sampling
Flow
S6
Flow
S6A
N
0
20 m
Mid-channel bar stream sediment sampling
Flow
S10
Flow
S10A
Flow
S10D
N
0
100 m
B
N
Proximal
Medial
Distal
S
Merapi Stratovolcano
Indian Ocean
Channel-side bar
Point bar
Mid-channel bar
Estuary
S1
S2
S3
S4
S5
S6
S7
S8
S9
S10
S11
S12
Elevation (m)
2250
2000
1750
1500
1250
1000
750
500
250
0
5
10
15
20
25
30
35
40
45
50
55
Distance (km)
Indian Ocean

Figure 4. Sampling methodology according to their channel bar type (Fig. 4A). The sampling locations are plotted with elevation and distance from source to sink (Fig. 4B). Notice the contrast of slope gradient between proximal – medial (S1 – S5) compared to medial – distal (S6 – S12).

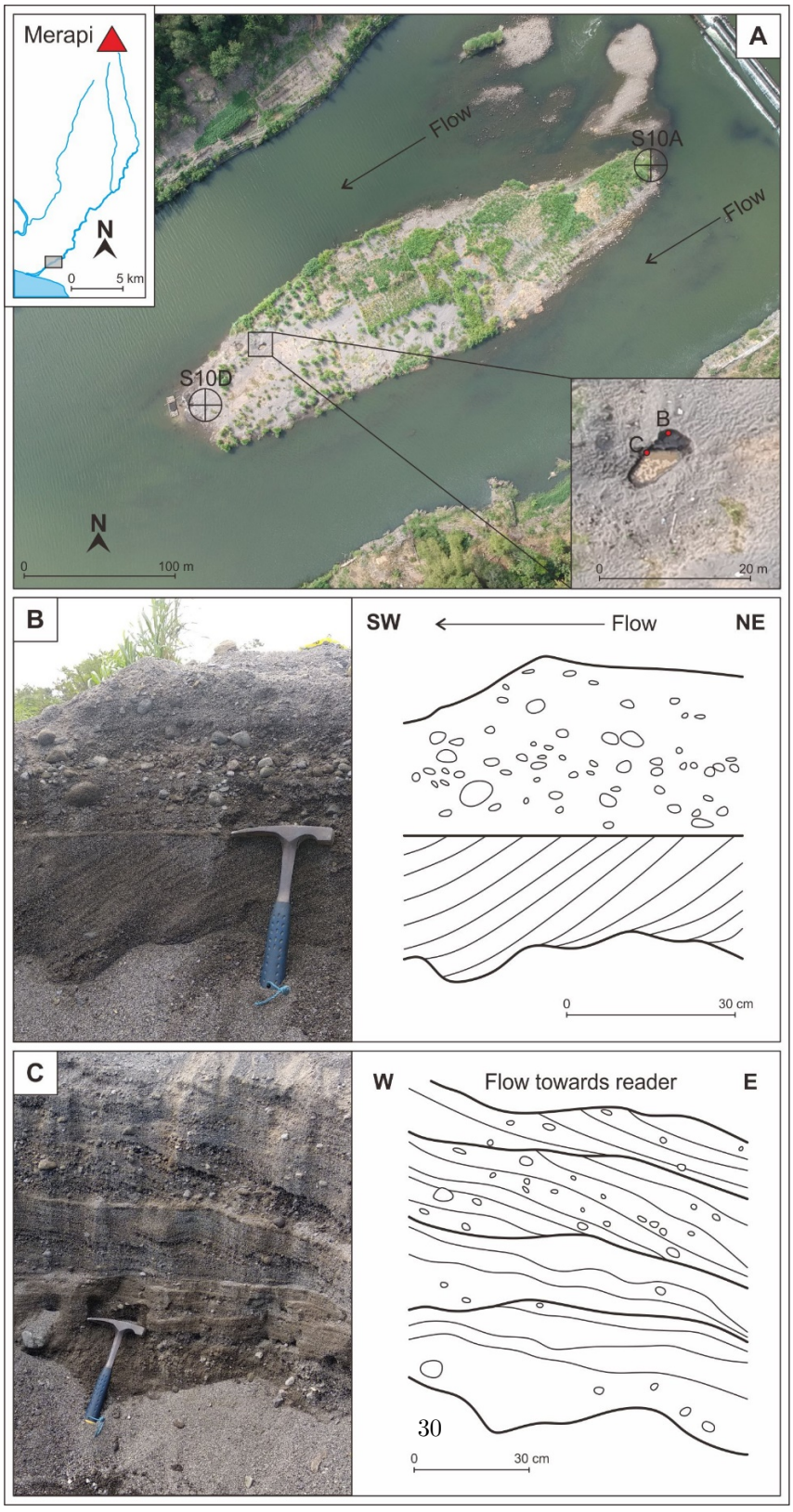
Merapi
N
0
5 km
A
Flow
S10A
Flow
S10D
B
C
N
0
100 m
0
20 m
B
SW
Flow
NE
0
30 cm
C
W
Flow towards reader
E
0
30 cm

Figure 5. Mid-channel bar formed in S10 sampling location. Notice the sedimentary structure shown in the trench (Fig. 5A), formed by the unconsolidated black sands (Fig. 5B and 5C). This location is mined by the locals for their iron-rich sand used for construction materials.

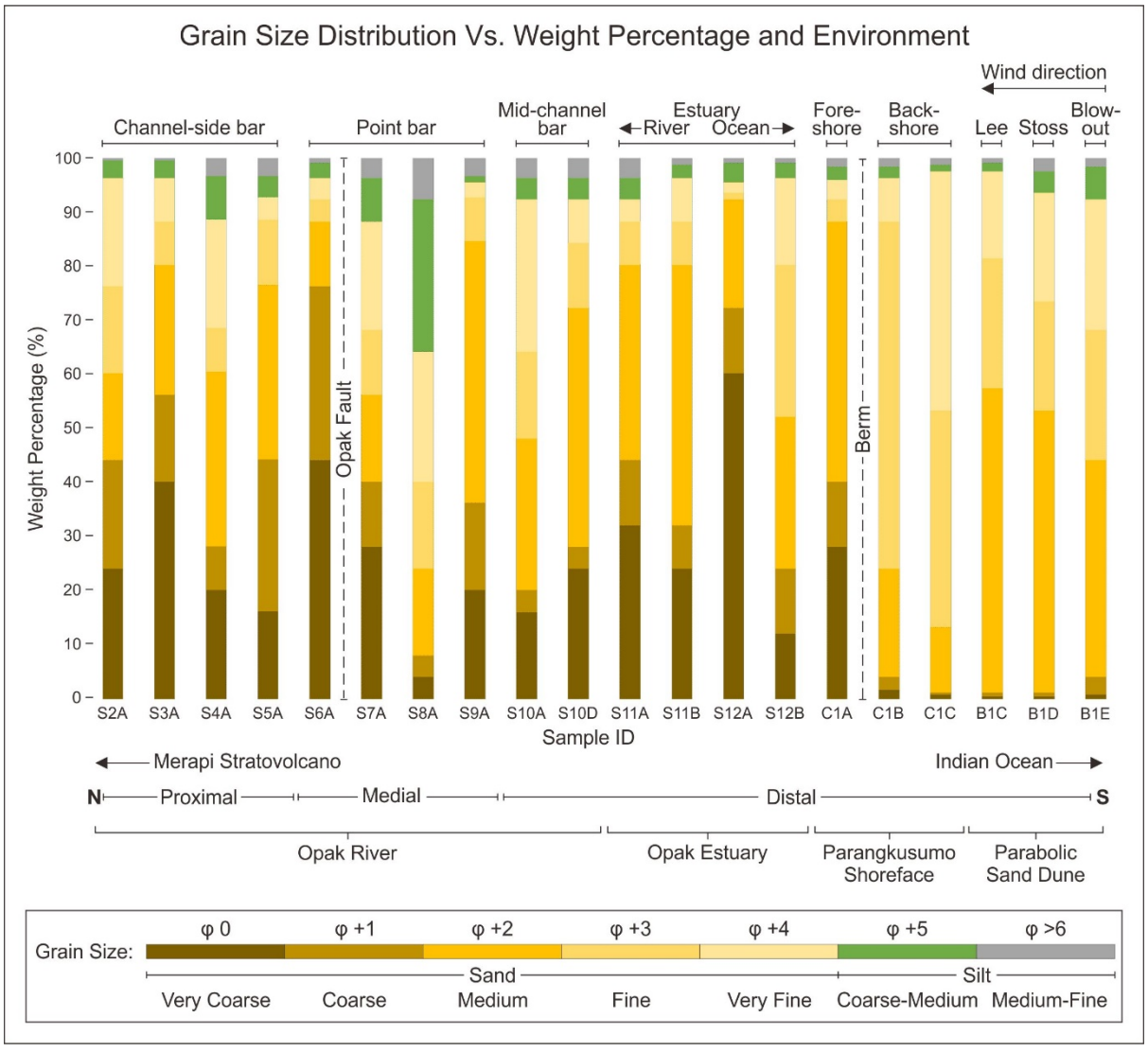

Figure 6. Grain size distribution from source to sink with its associated environments. Notice the inclusion of geomorphological expression such as Opak Fault and Berm which affect the distribution of grain size, and the prevailing wind direction for sand dune samples.

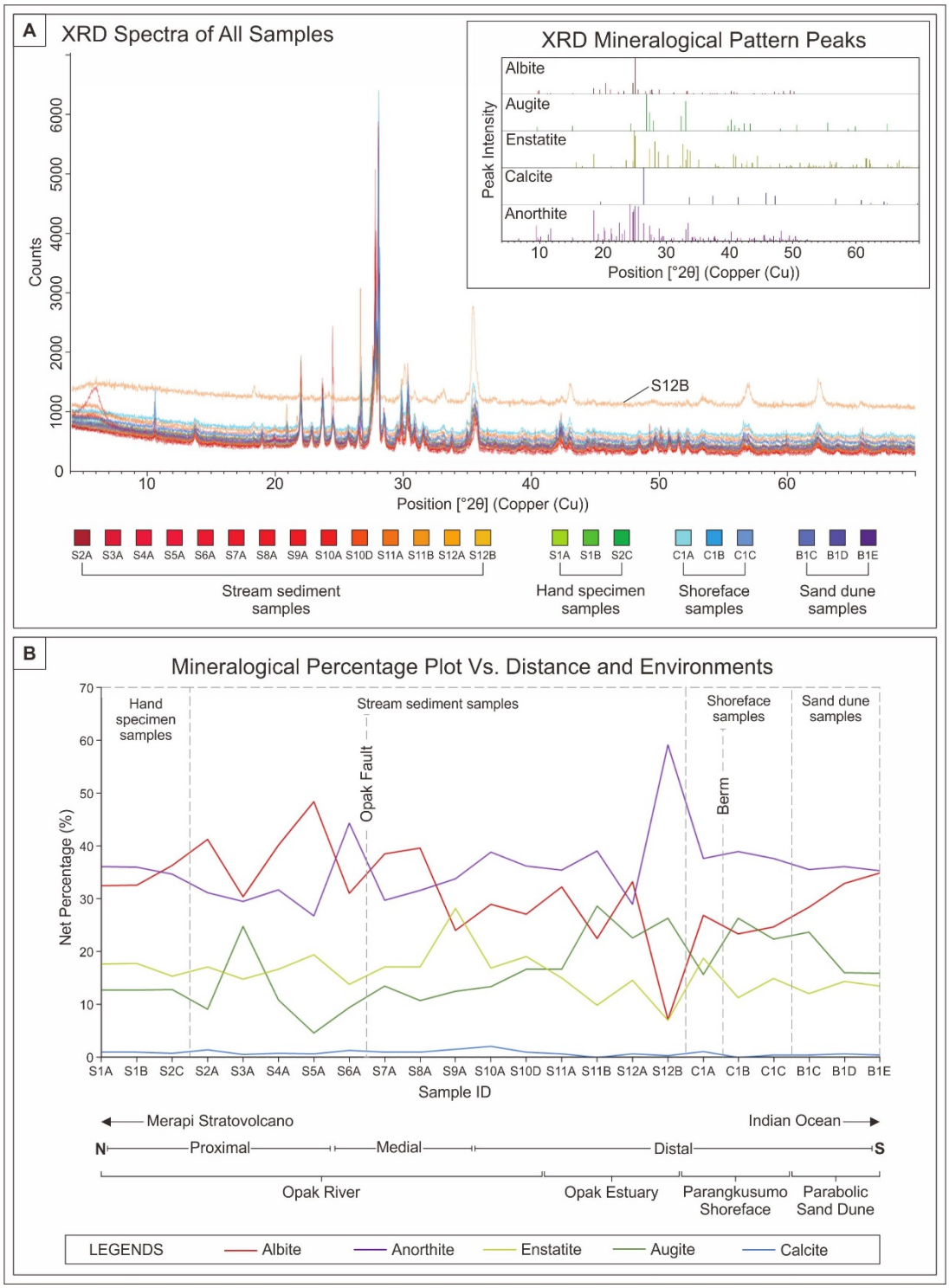
A
XRD Spectra of All Samples
XRD Mineralogical Pattern Peaks
Albite
Augite
Enstatite
Calcite
Anorthite
Peak Intensity
Position [°2θ] (Copper (Cu))
Counts
S12B
S2A S3A S4A S5A S6A S7A S8A S9A S10A S10D S11A S11B S12A S12B
S1A S1B S2C
C1A C1B C1C
B1C B1D B1E
Stream sediment samples
Hand specimen samples
Shoreface samples
Sand dune samples
B
Mineralogical Percentage Plot Vs. Distance and Environments
Hand specimen samples
Stream sediment samples
Shoreface samples
Sand dune samples
Opak Fault
Berm
Net Percentage (%)
Sample ID
Merapi Stratovolcano
Indian Ocean
N
Proximal
Medial
Distal
S
Opak River
Opak Estuary
Parangkusumo Shoreface
Parabolic Sand Dune
LEGENDS
Albite
Anorthite
Enstatite
Augite
Calcite

Figure 7. XRD spectra of all samples and the identified peaks for each minerals (Fig. 7A). Notice the distinct intensity represented by higher counts for sample S12B. The mineralogical pattern peaks shows 5 distinct minerals, which are albite, augite, enstatite, calcite, and anorthite. Plotting of mineralogical net percentage value in accordance with distance of sedimentation and the associated environments (Fig. 7B). Calcite is recorded to have the least amount of content, whereas albite and anorthite dominates the bulk mineralogical composition from proximal to distal.

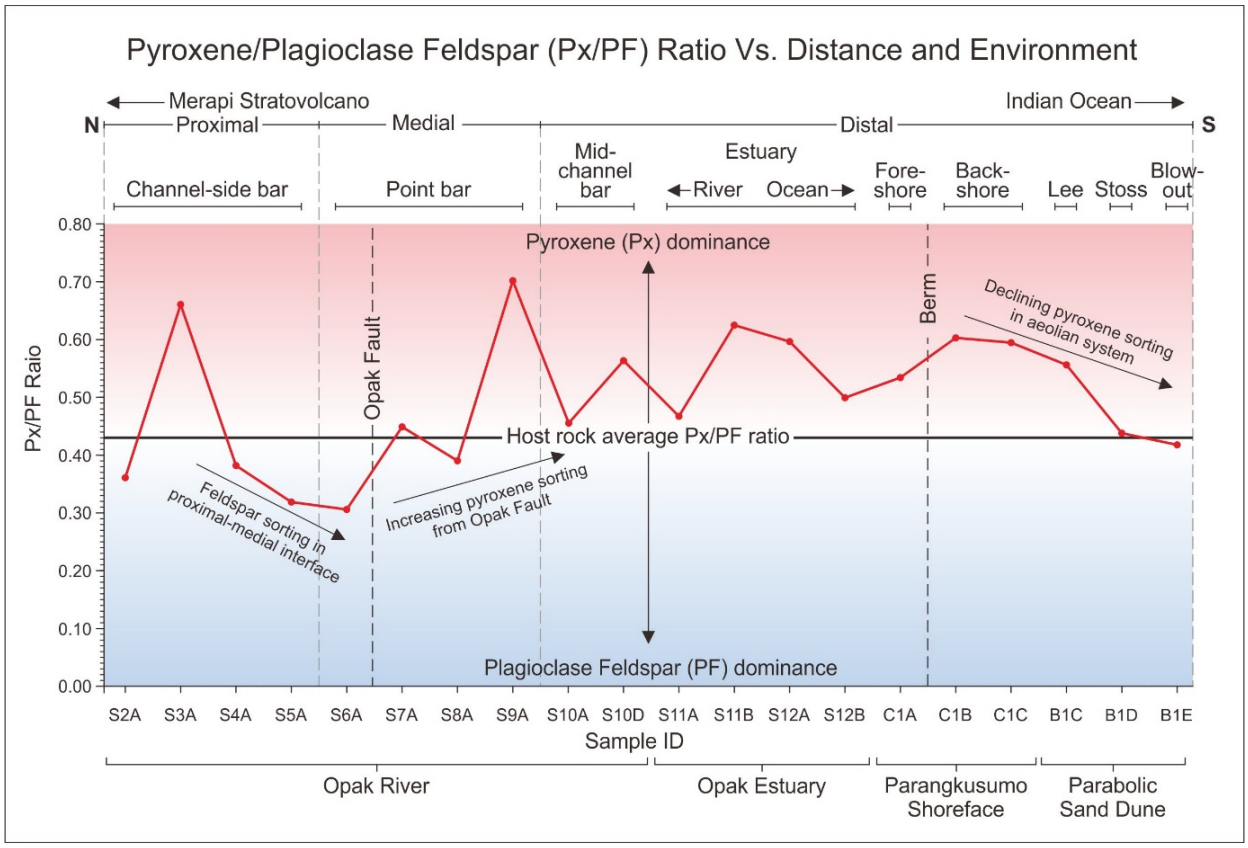

Figure 8. Pyroxene/Plagioclase Feldspar (Px/PF) ratio plot against depositional distance and environment. Note the presence of Opak Fault and Shoreface's berm in dashed line.

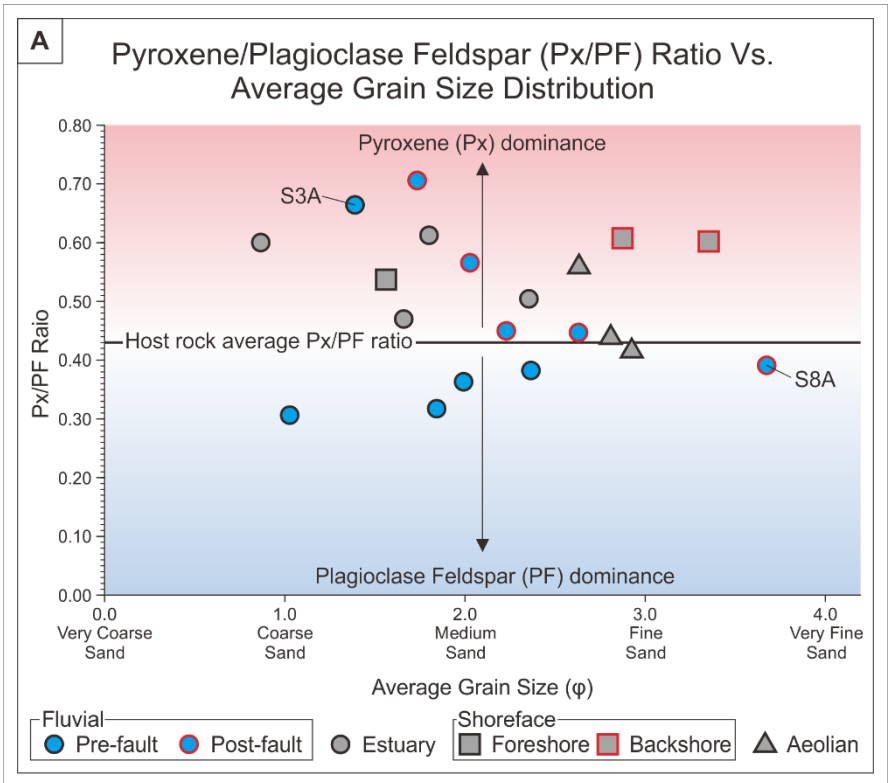
A
Pyroxene/Plagioclase Feldspar (Px/PF) Ratio Vs.
Average Grain Size Distribution
Pyroxene (Px) dominance
Plagioclase Feldspar (PF) dominance
Host rock average Px/PF ratio
S3A
S8A
Px/PF Raio
0.80
0.70
0.60
0.50
0.40
0.30
0.20
0.10
0.00
0.0 Very Coarse Sand
1.0 Coarse Sand
2.0 Medium Sand
3.0 Fine Sand
4.0 Very Fine Sand
Average Grain Size (φ)
Fluvial
Pre-fault
Post-fault
Estuary
Shoreface
Foreshore
Backshore
Aeolian

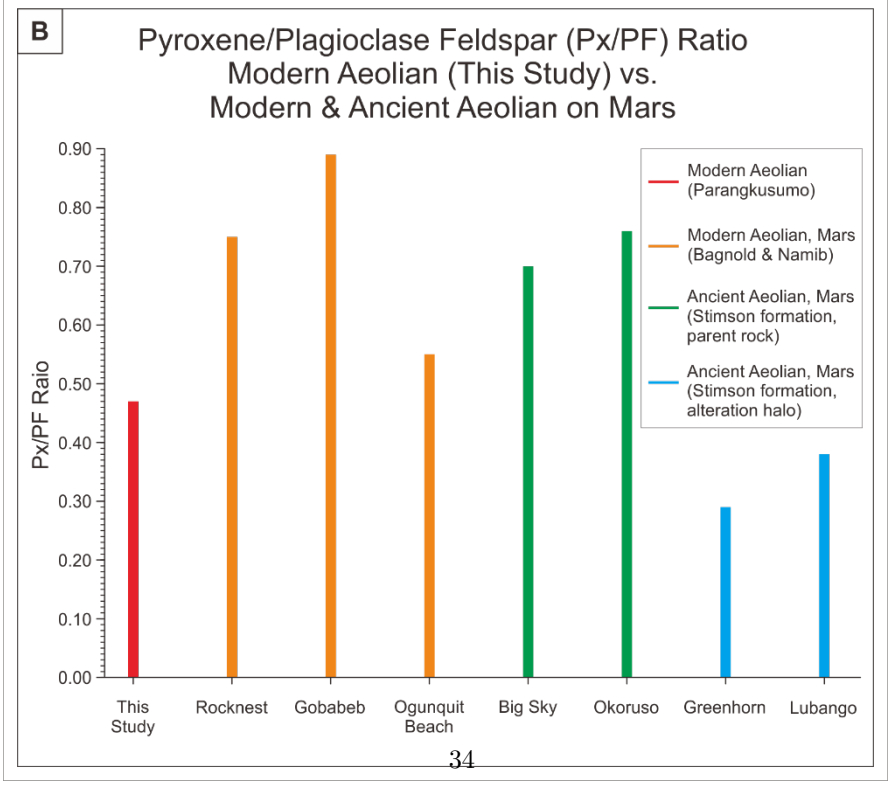
B
Pyroxene/Plagioclase Feldspar (Px/PF) Ratio
Modern Aeolian (This Study) vs.
Modern & Ancient Aeolian on Mars
Px/PF Raio
0.90
0.80
0.70
0.60
0.50
0.40
0.30
0.20
0.10
0.00
Modern Aeolian (Parangkusumo)
Modern Aeolian, Mars (Bagnold & Namib)
Ancient Aeolian, Mars (Stimson formation, parent rock)
Ancient Aeolian, Mars (Stimson formation, alteration halo)
This Study
Rocknest
Gobabeb
Ogunquit Beach
Big Sky
Okoruso
Greenhorn
Lubango

Figure 9. A plot of pyroxene/plagioclase feldspar (Px/PF) ratio against average grain size and depositional environment (Fig. 9A). Comparisons between this study's modern aeolian Px/PF ratio with modern and ancient aeolian found on Gale Crater (Fig. 9B).

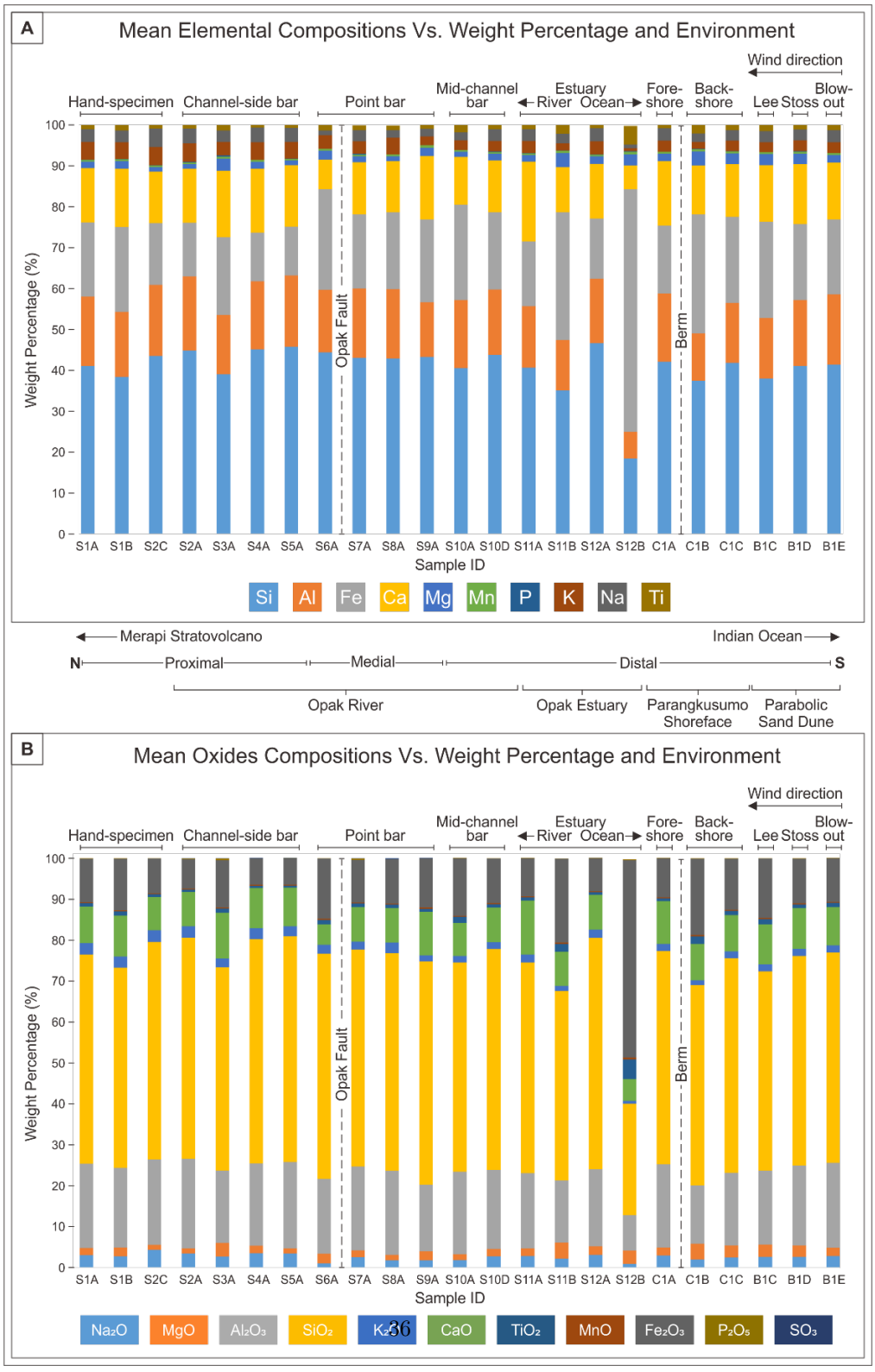
A
Mean Elemental Compositions Vs. Weight Percentage and Environment
Wind direction
Hand-specimen
Channel-side bar
Point bar
Mid-channel bar
Estuary
River
Ocean
Fore-shore
Back-shore
Lee
Stoss
Blow-out
Weight Percentage (%)
Opak Fault
Berm
S1A S1B S2C S2A S3A S4A S5A S6A S7A S8A S9A S10A S10D S11A S11B S12A S12B C1A C1B C1C B1C B1D B1E
Sample ID
Si Al Fe Ca Mg Mn P K Na Ti
Merapi Stratovolcano
Indian Ocean
N
Proximal
Medial
Distal
S
Opak River
Opak Estuary
Parangkusumo Shoreface
Parabolic Sand Dune
B
Mean Oxides Compositions Vs. Weight Percentage and Environment
Wind direction
Hand-specimen
Channel-side bar
Point bar
Mid-channel bar
Estuary
River
Ocean
Fore-shore
Back-shore
Lee
Stoss
Blow-out
Weight Percentage (%)
Opak Fault
Berm
S1A S1B S2C S2A S3A S4A S5A S6A S7A S8A S9A S10A S10D S11A S11B S12A S12B C1A C1B C1C B1C B1D B1E
Sample ID
Na2O MgO Al2O3 SiO2 K2O CaO TiO2 MnO Fe2O3 P2O5 SO3

Figure 10. Mean elemental (Fig. 10A) and oxides (Fig. 10B) plot with distance and environments derived from XRF. Notice the abundance for Fe and Fe_2O_3 in the sample S12B compared to the rest of the samples.

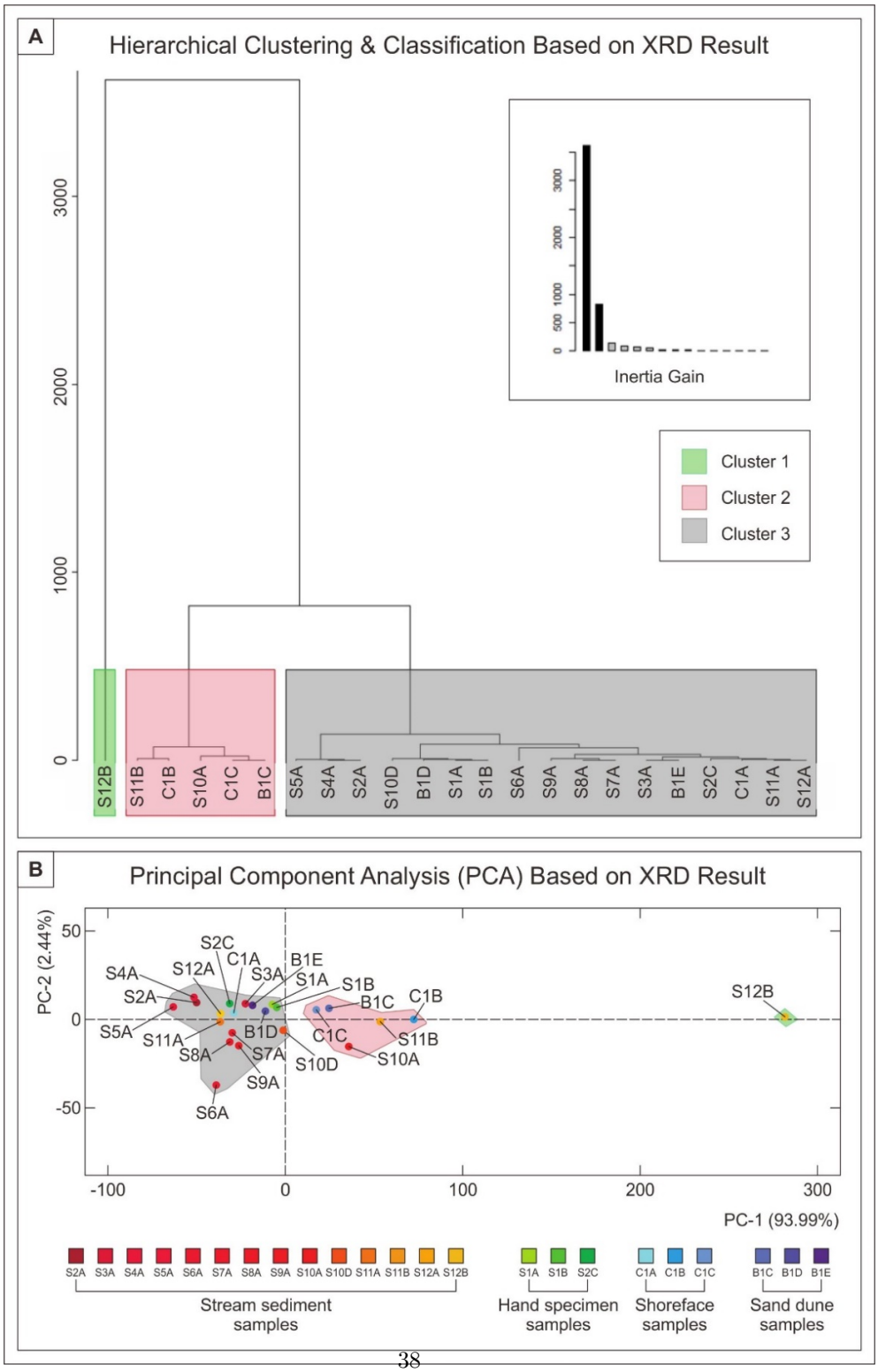
A
Hierarchical Clustering & Classification Based on XRD Result
3000
2000
1000
0
Inertia Gain
Cluster 1
Cluster 2
Cluster 3
S12B
S11B
C1B
S10A
C1C
B1C
S5A
S4A
S2A
S10D
B1D
S1A
S1B
S6A
S9A
S8A
S7A
S3A
B1E
S2C
C1A
S11A
S12A
B
Principal Component Analysis (PCA) Based on XRD Result
PC-2 (2.44%)
50
0
-50
-100
100
200
300
PC-1 (93.99%)
S2C
C1A
B1E
S4A
S12A
S3A
S1A
S1B
S2A
B1C
C1B
S5A
S11A
B1D
C1C
S11B
S8A
S7A
S10D
S10A
S9A
S6A
S12B
S2A S3A S4A S5A S6A S7A S8A S9A S10A S10D S11A S11B S12A S12B
Stream sediment samples
S1A S1B S2C
Hand specimen samples
C1A C1B C1C
Shoreface samples
B1C B1D B1E
Sand dune samples

Figure 11. Hierarchical Clustering on Principal Components (HCPC) dendogram (Fig. 11A) and Principal Component Analysis (PCA) plot (Fig. 11B) from geochemical analysis. Notice the three distinctive clusters in the dendogram represented in green, red, and black, and PC-1 correlation value of 93.99%.

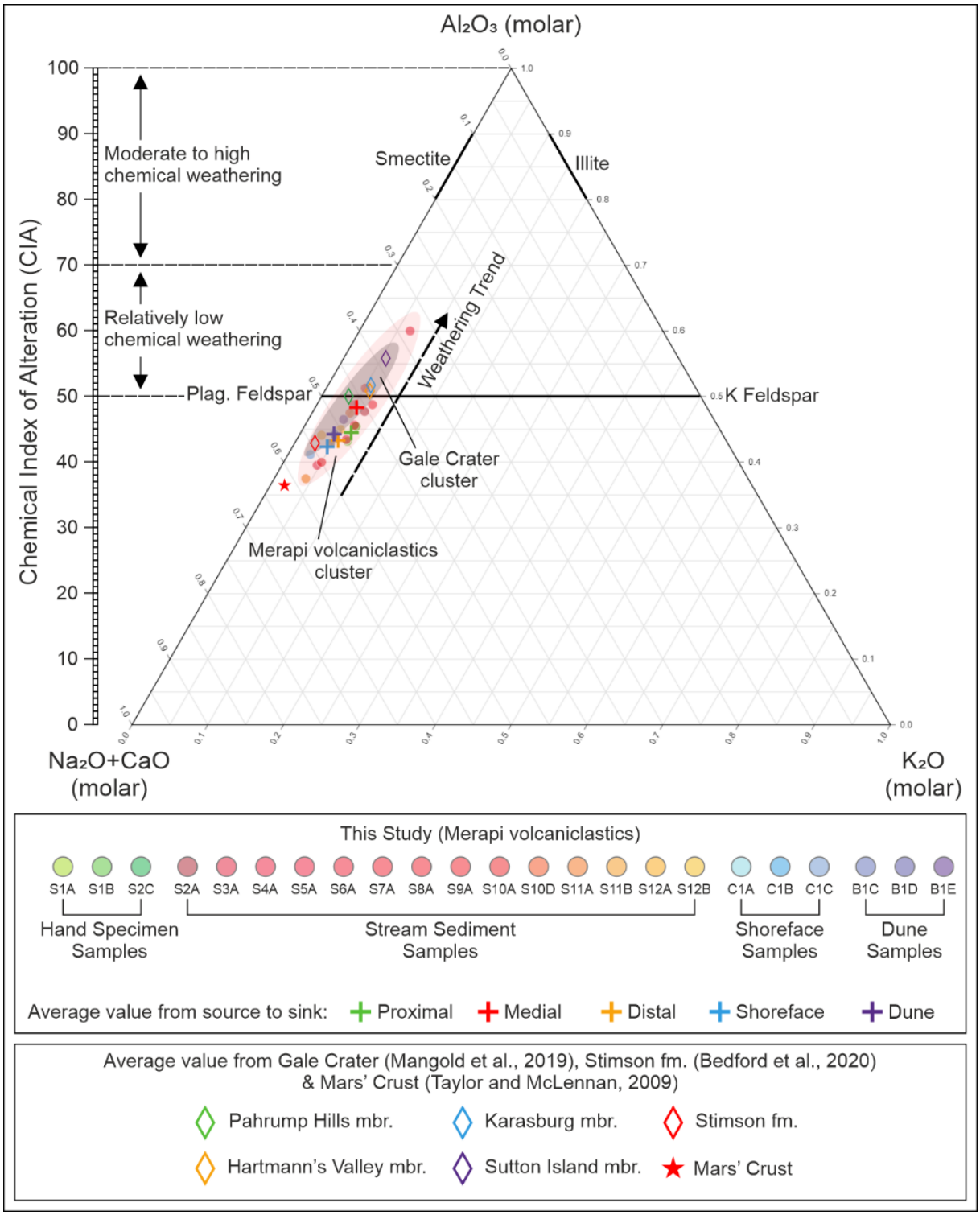
Al₂O₃ (molar)
Chemical Index of Alteration (CIA)
Na₂O+CaO (molar)
K₂O (molar)
Moderate to high chemical weathering
Relatively low chemical weathering
Plag. Feldspar
K Feldspar
Smectite
Illite
Weathering Trend
Gale Crater cluster
Merapi volcaniclastics cluster
This Study (Merapi volcaniclastics)
S1A S1B S2C S2A S3A S4A S5A S6A S7A S8A S9A S10A S10D S11A S11B S12A S12B C1A C1B C1C B1C B1D B1E
Hand Specimen Samples
Stream Sediment Samples
Shoreface Samples
Dune Samples
Average value from source to sink: Proximal Medial Distal Shoreface Dune
Average value from Gale Crater (Mangold et al., 2019), Stimson fm. (Bedford et al., 2020) & Mars' Crust (Taylor and McLennan, 2009)
Pahrump Hills mbr.
Karasburg mbr.
Stimson fm.
Hartmann's Valley mbr.
Sutton Island mbr.
Mars' Crust

Figure 12. Ternary A-CN-K diagram of Merapi volcaniclastics in comparison with Gale Crater (Mangold et al., 2019), Stimson fm (Bedford et al., 2020) and Mars' crust (Taylor and McLennan, 2009). CIA value is plotted as a vertical axis within the A-CN-K diagram. Notice the weathering trend of the samples and the clustering of our study (pale red shade) with the Gale Crater samples (pale grey shade).

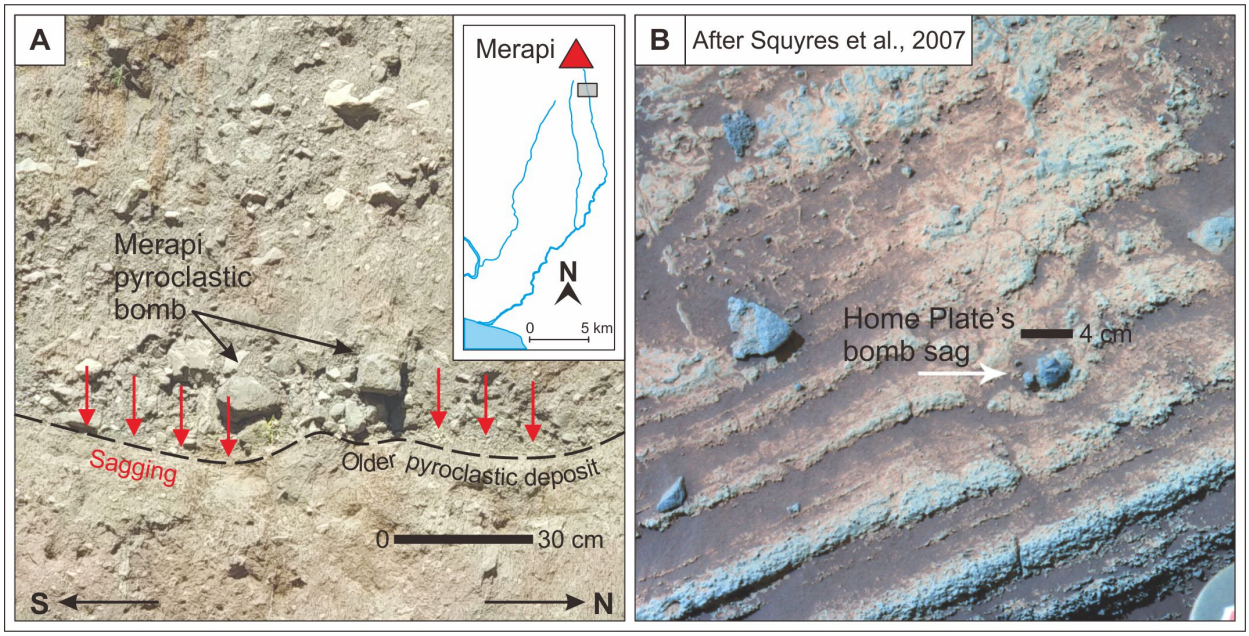

Figure 13. Comparison between Merapi's bomb sag in the proximal site (A) with Home Plate's bomb sag in Gusev Crater (B).

Open Research Availability Statement

The data provided in this research is currently available to download in supplementary section for peer-review purpose, since data archiving is in progress in EarthChem and will be available upon manuscript acceptance.

References

Aini, L. N., Soenarminto, B. H., Hanudin, E., Sartohadi, J. (2019). Plant nutritional potency of recent volcanic materials from the southern flank of mt. Merapi, Indonesia. Bulgarian Journal of Agricultural Science, 25 (No 3) 2019, 527–533

Alemanno, Giulia. (2018). Study of the fluvial activity on Mars through mapping, sediment transport modelling and spectroscopic analyses. PhD dissertation thesis, Cornell University, Earth and Planetary Astrophysics. DOI: arXiv:1805.02208v1

Anderson, R., J.C. Bridges, A. Williams, L. Edgar, A. Ollila, J. Williams, M.

Nachon, N. Mangold, M. Fisk, J. Schieber, S. Gupta, G. Dromart, R. Wiens, S. Le Mouélic, O. Forni, N. Lanza, A. Mezzacappa, V. Sautter, D. Blaney, B. Clark, S. Clegg, O. Gasnault, J. Lasue, R. Léveillé, E. Lewin, K.W. Lewis, S. Maurice, H. Newsom, S.P. Schwenzer, and D. Vaniman. (2015). ChemCam results from the Shaler outcrop in Gale Crater, Mars, Icarus, 249:2-21, DOI: 10.1016/j.icarus.2014.07.025,

Andreastuti, S.D., Alloway, B.V., Smith, I.E.M. 2000. A detailed tephrostratigraphic framework at Merapi Volcano, Central Java, Indonesia: implications for eruption predictions and hazard assessment. Journal of Volcanology and Geothermal Research 100, 51–67, DOI: 10.1016/S0377-0273(00)00133-5

Bedford, C. C., Bridges, J. C., Schwenzer, S. P., Wiens, R. C., Rampe, E. B., Frydenvang, J., and Gasda, P. J. (2019). Alteration trends and geochemical source region characteristics preserved in the fluviolacustrine sedimentary record of Gale crater, Mars. Geochimica et Cosmochimica Acta 246, p.234–266. DOI: 10.1016/j.gca.2018.11.031

Bedford, C. C., Schwenzer, S. P., Bridges, J. C., Banham, S., Wiens, R. C., Gasnault, O., Rampe, E. B., Frydenvang, J., and Hasda, P. J. (2020). Geochemical variation in the Stimson formation of Gale Crater: Provenance, mineral sorting, and a comparison with modern Martian dunes. Icarus 341, 113622. DOI: 10.1016/j.icarus.2020.113622

Berthommier, P., Camus, G. (1991). Les eruptions historiques du Merapi (Centre Java Indonesie). Bull. Sect. Volcanol. Soc. Geol. Fr. 23, 1-11.

Bradley, B. A., Sakimoto, S. E. H., Frey, H., Zimbelman, J. R., Medusae Fossae Formation: New perspectives from Mars Global Surveyor, J. Geophys. Res., 107(E8), DOI: 10.1029/2001JE001537

Bridges, N., Ayoub, F., Avouac, JP., Leprince, S., Lucas, A., and Mattson, S. (2012). Earth-like sand fluxes on Mars. Nature 485, 339–342. DOI: 10.1038/nature11022

Brož, P. and Hauber, E. (2012). A unique volcanic field in Tharsis, Mars: Pyroclastic cones as evidence for explosive eruptions, Icarus, Volume 218, Issue 1, p88-99, DOI:10.1016/j.icarus.2011.11.030.

Camus, G., Gourgaud, A., Mossand-Berthommier, P.-C., Vincent, P.-M. (2000). Merapi (central Java, Indonesia): an outline of the structural and magmatological evolution, with a special emphasis to the major pyroclastic events. J. Volcanol. Geotherm. Res., 100: 139-163.

Carr, M. H., and Head, J. W. (2003). Oceans on Mars: An assessment of the observational evidence and possible fate, J. Geophys. Res., 108, 5042, E5, DOI: 10.1029/2002JE001963

Carr, M. H. (2012). The fluvial history of Mars. Phil. Trans. R. Soc. A, 370, 2193–2215. DOI: 10.1098/rsta.2011.0500

Carter, R. W. G., Hesp, P. A. & Nordstrom, N. F. (1990). Erosional landforms in coastal dunes, in Coastal Dunes: Form and Process, eds. K. F. Nordstrom, N. Psuty & B. Carter (Brisbane, Australia: John Wiley and Son, 1990) 217–252.

Charbonnier, S. J., Gertisser, R. (2008). Field observations and surface characteristics of pristine block-and-ash flow deposits from the 2006 eruption of Merapi volcano, Java, Indonesia. J. Volcanol. Geotherm. Res., 177: 971-982.

Carter, R. W. G., Hesp, P. A. & Nordstrom, N. F. (1990). Erosional landforms in coastal dunes, in Coastal Dunes: Form and Process, eds. K. F. Nordstrom, N. Psuty & B. Carter (Brisbane, Australia: John Wiley and Son, 1990) 217–252.

Ciarletti, V., Corbel, C., Dolon, F., Jeangeot, A., Berthelier, J-J., Ney, R., Hamran, S. E., Plettemeier, D., and Caïs, P. (2017). A UHF step frequency GPR for the ESA EXOMARS mission. 10th International Congress of the Brazilian Geophysical Society & EXPOGEF 2007, Rio de Janeiro, Brazil, 19-23 November 2007. November 2007, 578-580, DOI: 10.1190/sbgf2007-113

Clifford, S. M., and Parker, T. J. (2001). The Evolution of the Martian Hydrosphere: Implications for the Fate of a Primordial Ocean and the Current State of the Northern Plains. Icarus, Vol 154, Issue 1, p. 40-79. DOI: 10.1006/icar.2001.6671

Czarnecki, S., Hardgrove, C., Gasda, P. J., Gabriel, T. S. J., Starr, M., Rice, M. S., et al. (2020). Identification and description of a silicic volcaniclastic layer in Gale crater, Mars, using active neutron interrogation. Journal of Geophysical Research: Planets, 125, e2019JE006180. DOI: 10.1029/2019JE006180

Deegan, F.M., Troll, V. R., Freda, C., Misiti, V., Chadwick, J.P., McLeod, C. L., and Davidson, J.P. (2010). Magma-Carbonate Interaction Processes and Associated CO2 Release at Merapi Volcano, Indonesia: Insights from Experimental Petrology. Journal of Petrology, Vol. 51, Number 5, p.1027-1051 2010. DOI: 10.1093/petrology/egq010

Di Achille, G., Hynek, B. M. (2010). Ancient ocean on Mars supported by global distribution of deltas and valleys. Nat. Geosci., 3 (7) (2010), pp. 459-463

Edgett, K. and Lancaster, N. (1993). Volcaniclastic Aeolian dunes: terrestrial examples and applications to Martian sands. Journal of Arid Environments. 25. 271–297. DOI: 10.1006/jare.1993.1061.

Edgett, K., Banham, S., Bennet, K., Edgar, L., Edwards, C., et al.. (2020). Extraformational sediment recycling on Mars. Geosphere, Geological Society of America, 2020, 16 (6), pp.1508-1537. DOI: ff10.1130/GES02244.1ff. ffhal-03104177f

Edwards, T. K. and Glysson, G. D. (1999). Field Methods for Measurement of Fluvial Sediment. Techniques of Water-Resources Investigations of the U.S. Geological Survey, Book 3, Applications of Hydraulics, Chapter C2. ISBN 0-607-89738-4.

Fassett, C. I., and Head, J. W. (2005). Fluvial sedimentary deposits on Mars: Ancient deltas in a crater lake in the Nili Fossae region, Geophys. Res. Lett., 32, L14201, DOI: 10.1029/2005GL023456.

Ghatan, G. J., and Zimbelman, J. R. (2006). Paucity of candidate coastal constructional landforms along proposed shorelines on Mars: Implications for a northern lowlands-filling ocean. Icarus, Vol 185, Issue 1, p. 171-196. DOI: 10.1016/j.icarus.2006.06.007

Goldberg, K., and Humayun, M. (2010). The applicability of the Chemical Index of Alteration as a paleoclimatic indicator: An example from the Permian of the Paraná Basin, Brazil. Palaeogeography, Palaeoclimatology, Palaeoecology, Volume 293, Issues 1–2, P. 175-183, DOI: 10.1016/j.palaeo.2010.05.015.

Greeley, R., and Guest, J. E. (1987). Geologic Map of the Eastern Equatorial Region of Mars. IMAP 1802-B. DOI: 10.3133/i1802B

Greeley, R., Lancaster, N., Lee, S., and Thomas, P. (1992). Martian aeolian processes, sediments, and features. The international journal of Mars science and exploration, February 1992.

Gregg, T. K. P., and Farley, M. A. (2006). Mafic pyroclastic flows at Tyrrhena Patera, Mars: Constraints from observations and models. Journal of Volcanology and Geothermal Research 155 (2006) 81–89. DOI:10.1016/j.jvolgeores.2006.02.008

Grotzinger, J.P., Arvidson, R.E., Bell, J.F., Calvin, W., Clark, B.C., Fike, D.A., Golombek, M., Greeley, R., Haldemann, A., Herkenhoff, K.E., Jolliff, B.L., Knoll, A.H., Malin, M., McLennan, S.M., Parker, T., Soderblom, L., Sohl-Dickstein, J.N., Squyres, S.W., Tosca, N.J., and Watters, W.A. (2005). Stratigraphy and sedimentology of a dry to wet eolian depositional system, Burns formation, Meridiani Planum, Mars. Earth and Planetary Science Letters 240 (2005) 11 –72. DOI: 10.1016/j.epsl.2005.09.039

Grotzinger, J. P. et al. (2014). A Habitable Fluvio-Lacustrine Environment at Yellowknife Bay, Gale Crater, Mars. Science, 343, DOI: 10.1126/science.1242777

Grotzinger, J. P. et al. (2015). Deposition, exhumation, and paleoclimate of an ancient lake deposit, Gale crater, Mars. Science, 350. DOI: 10.1126/science.aac7575.

Gulick, V. C., and Baker, V. R. (1990). Origin and evolution of valleys on Martian volcanoes. Jou. Geophys. Res. 95, 14,325– 14,344.

Hamran, Svein-Erik & Paige, David & Amundsen, Hans Erik Foss & Berger, Tor & Brovoll, Sverre & Carter, Lynn & Damsgard, Leif & Dypvik, Henning & Eide, Jo & Eide, Sigurd & Ghent, Rebecca & Helleren, Øystein & Kohler, Jack & Mellon, Mike & Nunes, Daniel & Plettemeier, Dirk & Rowe, Kathryn & Russell, Patrick & Øyan, Mats. (2020). Radar Imager for Mars' Subsurface Experiment—RIMFAX. Space Science Reviews. 216. 10.1007/s11214-020-00740-4.

Head, J. W. III., Hiesinger, H., Ivanov, M. A., Kreslavsky, M. A., Pratt, S., and Thomson, B. J. (1999). Possible Ancient Oceans on Mars: Evidence from MArs Orbiter Laser Altimeter Data. Science, Vol 286, Issue 5447, pp. 2134-2137. DOI: 10.1126/science.286.5447.2134

Hervé, Y., V. Ciarletti, A. Le Gall, C. Corbel, R. Hassen-Khodja, W.S. Benedix, D. Plettemeier, O. Humeau, A.J. Vieau, B. Lustrement, S. Abbaki, E. Bertran, L. Lapauw, V. Tranier, N. Oudart, F. Vivat, C. Statz, Y. Lu, S. Hegler, A. Hérique (2020). The WISDOM radar on board the ExoMars 2022 Rover: Characterization and calibration of the flight model, Planetary and Space Science, Volume 189, DOI: 10.1016/j.pss.2020.104939.

Hesp, P. A. (1999). The beach backshore and beyond, in Handbook of Beach and Shoreface Morphodynamics, ed. A. D. Short (Brisbane, Australia: John Wiley and Son, 1999).

Hesp, P. A. (2002). Foredunes and blowouts: Initiation, geomorphology and dynamics. Geomorphology 48, 245–268.

Hughes, C. M., Cardenas, B. T., Goudge, T. A., and Mohrig, D. (2019). Deltaic deposits indicative of a paleo-coastline at Aeolis Dorsa, Mars. Icarus, v317, p.442-453, doi: 10.1016/j.icarus.2018.08.009.

Hussain, M., Amao, A., Jin, G., and Al-Ramadan, K. (2018). Linking Geochemical and Mechanical Properties of Rock Samples Using New Non-Destructive Techniques. SPE Kingdom of Saudi Arabia Annual Technical Symposium and Exhibition, Dammam, Saudi Arabia, 23-26 April 2018. SPE-192347-MS.

Hooper, D. M., McGinnis, R. N., and Necsoiu, M. (2012). Volcaniclastic aeolian deposits at Sunset Crater, Arizona: terrestrial analogs for Martian dune forms. Earth Surf. Process. Landforms 37, 1090–1105 (2012), DOI: 10.1002/esp.3238

Horvath, D. G., Moitra, P., Hamilton, C. W., Craddock, R. A., and Andrews-Hanna, J. C. (2021). Evidence for geologically recent explosive volcanism in Elysium Planitia, Mars. Icarus, vol. 365, 114499. DOI: 10.1016/j.icarus.2021.114499

Kassambara, A., & Mundt, F. (2016). Factoextra: Extract and visualize the results of multivariate data analyses. R Package Version, 1(3).

Kaufhold, A., Halisch, M., Zacher, G., & Kaufhold, S. (2016). X-ray computed tomography investigation of structures in Opalinus Clay from large-scale to small-scale after mechanical testing. *Solid Earth*, 7(4), 1171–1183.

Kopp, H. & Flueh, E. & Petersen, Carl Jörg & Weinrebe, W. & Wittwer, A. 2006. The Java margin revisited: Evidence for subduction erosion off Java. Earth and Planetary Science Letters 242(1):130-142, DOI: 10.1016/j.epsl.2005.11.036.

Lapotre, M. G. A., and Rampe, E. B. (2018). Curiosity's Investigation of the Bagnold Dunes, Gale Crater: Overview of the Two-Phase Scientific Campaign

and Introduction to the Special Collection. Geophysical Research Letters, 45, 10,200–10,210. DOI: 10.1029/2018GL079032.

Lavigne, F., Thouret, J. C., Voight, B., Suwa, H., and Sumaryono, A. (2000). Lahars at Merapi Volcano, Central Java: an overview. Journal of Volcanology and Geothermal Research 100, 423–456, DOI: 10.1016/S0377-0273(00)00150-5

Le Deit, L., Mangold, N., Forni, O., Cousin, A., Lasue, J., Schröder, S., Wiens, R. C., Sumner, D., Fabre, C., Stack, K. M., Anderson, R. B., Blaney, D., Clegg, S., Dromart, G., Fisk, M., Gasnault, O., Grotzinger, J. P., Gupta, S., Lanza, N. Le Mouélic, S., Maurice, S., McLennan, S. M., Meslin, P. -Y., Nachon, M., Newsom, H., Payré, V., Rapin, W., Rice, M., Sautter, V., and Treiman, A. H. (2016), The potassic sedimentary rocks in Gale Crater, Mars, as seen by ChemCam on board Curiosity, J. Geophys. Res. Planets, 121, 784– 804, DOI: 10.1002/2015JE004987.

Lê, S., Josse, J., Husson, F., & others. (2008). FactoMineR: an R package for multivariate analysis. Journal of Statistical Software, 25(1), 1–18.

Lorenz, V. (1974). Vesiculated tuffs and associated features. Sedimentology 21, 273–291.

Malin, M. C., and Edgett, K. S. (1999). Oceans or seas in the Martian northern lowlands: High resolution imaging tests of proposed coastlines. Geophysical Research Letters, Vol. 26, Issue 19, p. 3049-3052. DOI: 10.1029/1999GL002342

Mangold, N., Dehouck, E., Fedo, C., Forni, O., Achilles, C., Bristow, T., et al. (2019). Chemical alteration of fine-grained sedimentary rocks at Gale crater. Icarus, 321, 619–631. DOI: 10.1016/j.icarus.2018.11.004

Masselink, G.; Short, A. D. (1993). The effect of tidal range on beach morphodynamics and morphology: a conceptual beach model. Journal of Coastal Research. 9 (3): 785–800. ISSN 0749-0208

McSween Jr, H. Y., Taylor, G. J., and Wyatt, M. B. (2009). Elemental Composition of the Martian Crust. Science, Vol. 324, Issue 5928, pp. 736-739, DOI: 10.1126/science.1165871

Morris, R., Vaniman, D., Blake, D., Gellert, R., Chipera, S., Rampe, E., Ming, D., Morrison, S., Downs, R., Treiman, A., Yen, A., Grotzinger, J., Achilles, C., Bristow, T., Crisp, J., Desmarais, D., Farmer, J., Fendrich, K., Frydenvang, J., Schwenzer, S. (2016). Silicic volcanism on Mars evidenced by tridymite in high-SiO 2 sedimentary rock at Gale crater. Proceedings of the National Academy of Sciences. 113. 201607098. DOI: 10.1073/pnas.1607098113.

Morrison, S. M., Downs, R. T., Blake, D.F., Vaniman, D. T., Ming, D. W., Hazen, R. M., Treiman, A. H., Achilles, C. N., Yen, A. S., Morris, R. V., Rampe, E. B., Bristow, T. F., Chipera, S. J., Sarrazin, P. C., Gellert, R., Fendrich, K. V., Morookian, J. M., Farmer, J. D., Des Marais, D. J., and Craig, P. I. (2018). Crystal chemistry of martian minerals from Bradbury Landing through

Naukluft Plateau, Gale crater, Mars. American Mineralogist; 103 (6): 857–871. DOI: https://doi.org/10.2138/am-2018-6124

Nesbitt, H., & Young, G. M. (1982). Early Proterozoic climates and plate motions inferred from major element chemistry of lutites. Nature, 299(5885), 715-717.

Payré, V., Siebach, K. L., Dasgupta, R., Udry, A., Rampe, E. B., and Morrison, S. M. (2020). Constraining ancient magmatic evolution on Mars using crystal chemistry of detrital igneous minerals in the sedimentary Bradbury group, Gale crater, Mars. Journal of Geophysical Research: Planets, 125, e2020JE006467. DOI: 10.1029/2020JE006467

Perillo, G. M. E. (1995). Definitions and geomorphic classifications of estuaries. In Geomorphology and Sedimentology of Estuaries. Developments in Sedimentology 53. Ed. Perillo, G. M. E. (New York: Elsevier Science 1995). 17-47.

Peterson, B. G., Carl, P., Boudt, K., Bennett, R., Ulrich, J., Zivot, E., Lestel, M., Balkissoon, K., & Wuertz, D. (2014). PerformanceAnalytics: Econometric tools for performance and risk analysis. R Package Version, 1(3541), 107.

Preece, K., Barclay, J., Gertisser, R., and Herd, R. (2013). Textural and micro-petrological variations in the eruptive products of the 2006 dome-forming eruption of Merapi volcano, Indonesia: Implications for sub-surface processes. Journal of Volcanology and Geothermal Research. 261. 98-120. DOI: 10.1016/j.jvolgeores.2013.02.006.

Rahardjo, W., Sukandarrumidi, and Rosidi, H. M. D. (1995). Geological Map of the Yogyakarta Sheet, Jawa. Geological Survey of Indonesian Ministry of Mines, Geological Research and Development Centre, 2nd edition.

Rampe, E. B., Blake, D. F., Bristow, T. F., Ming, D. W., Vaniman, D. T., Morris, R. V., Achilles, C. N., Chipera, S. J., Morrison, S. M., Tu, V. M., Yen, A. S., Castle, N., Downs, G. W., Downs, R. T., Grotzinger, J. P., Hazen, R. M., Treiman, A. H., Peretyazhko, T. S., Des Marais, D. J., Walroth, R. C., Craig, P. I., Crisp, J. A., Lafuente, B., Morookian, J. M., Sarrazin, P. C., Thorpe, M. T., Bridges, J. C., Edgar, L. A., Fedo, C. M., Freissinet, C., Gellert, R., Mahaffy, P. R., Newsome, H. E., Johnson, J. R., Kah, L. C., Siebach, K. L., Schieber, J., Sun, V. Z., Vasavada, A. R., Wellington, D., Wiens, R. C. (2020). Mineralogy and geochemistry of sedimentary rocks and eolian sediments in Gale crater, Mars: A review after six Earth years of exploration with Curiosity, Geochemistry, Volume 80, Issue 2. DOI: /10.1016/j.chemer.2020.125605.

Raschke, U., Schmitt, R. T., & Reimold, W. U. (2013). Petrography and geochemistry of impactites and volcanic bedrock in the ICDP drill core D1c from Lake El'gygytgyn, NE Russia. Meteoritics & Planetary Science, 48(7), 1251–1286.

Ray, R.D., Egbert, G.D., and Erofeeva, S. Y. (2005). A Brief Overview of Tides in the Indonesian Seas. Journal of the Oceanography Society, Oceanography

Vol. 18, No. 4, Dec. 2005

Rodriguez, E., Morris, C., Belz, J., Chapin, E., Martin, J., Daffer, W., & Hensley, S. (2005). An assessment of the SRTM topographic products.

Sara, M. J. (2017). Dyngjusandur sand sheet, Iceland, as a depositional analog to the Stimson Fm. in Gale Crater, Mars. MS (Master of Science) thesis, University of Iowa. doi: 10.17077/etd.25rc5gg2

Sautter, V., Toplis, M. J., Wiens, R. C., Cousin, A., Fabre, C., Gasnault, O., ... & Wray, J. J. (2015). In situ evidence for continental crust on early Mars. Nature Geoscience, 8(8), 605-609.

Sautter, V., Toplis, M. J., Beck, P., Mangold, N., Wiens, R., Pinet, P., ... & Le Mouélic, S. (2016). Magmatic complexity on early Mars as seen through a combination of orbital, in-situ and meteorite data. Lithos, 254, 36-52.

Schmidt, M. E., Campbell, J.L., Gellert, R., Perrett, G. M., Treiman, A. H., Blaney, D. L., Olilla, A., Calef III, F. J., Edgar, L., Elliott, B. E., Grotzinger, J., Hurowitz, J. C., Ehlmann, B. L., Forni, O., Leshin, L. A., Lewis, K. W., McLennan, S. M., Ming, D. W., Newsom, H., Pradler, I., Squyres, S. W., Stolper, E. M., Thompson, L., VanBommel, S., and Wiens, R. C. (2014). Geochemical diversity in first rocks examined by the Curiosity Rover in Gale Crater: Evidence for and significance of an alkali and volatile-rich igneous source. Journal of Geophysical Research: Planets, Vol. 119, 64–81, DOI: 10.1002/2013JE004481

Scott, D. H., and Tanaka, K. L. (1986). Geologic Map of the Western Equatorial Region of Mars. IMAP 1802-A. DOI: 10.3133/i1802A

Seelos, K. D., Arvidson, R. E., Jolliff, B. L., Chemtob, S. M., Morris, R. V., Ming, D. W., and Swayze, G. A. (2010), Silica in a Mars analog environment: Ka'u Desert, Kilauea Volcano, Hawaii, J. Geophys. Res., 115, E00D15, DOI: 10.1029/2009JE003347.

Siebach, K. L., Baker, M. B., Grotzinger, J. P., McLennan, S. M., Gellert, R., Thompson, L.M., and Hurowitz, J. A. (2017). Sorting out compositional trends in sedimentary rocks of the Bradbury group (Aeolis Palus), Gale crater, Mars, J. Geophys. Res. Planets, 122, 295–328, DOI: 10.1002/2016JE005195

Sloss, C. R., Shepherd, M. & Hesp, P. (2012a). Coastal Dunes: Geomorphology. Nature Education Knowledge 3(10):2.

Sloss, C. R., Hesp, P. & Shepherd, M. (2012b) Coastal Dunes: Aeolian Transport. Nature Education Knowledge 3(10):21

Squyres, S. W., et al. (2006), Overview of the Opportunity Mars Exploration Rover Mission to Meridiani Planum: Eagle Crater to Purgatory Ripple, J. Geophys. Res., 111, E12S12, doi:10.1029/2006JE002771.

Squyres, S. W., O. Aharonson, B.C. Clark, B. A. Cohen, L. Crumpler, P. A. de Souza, W. H. Farrand, R. Gellert, J. Grant, J. P. Grotzinger, A. F. C. Haldemann, J. R. Johnson, G. Klingelhöfer, K. W. Lewis, R. Li, T. McCoy,

A. S. McEwen, H. Y. McSween, D. W. Ming, J. M. Moore, R. V. Morris, T. J. Parker, J. W. Rice Jr., S. Ruff, M. Schmidt, C. Schröder, L. A. Soderblom and A. Yen. (2007). Pyroclastic Activity at Home Plate in Gusev Crater, Mars. Science 316 (5825), 738-742. DOI: 10.1126/science.1139045

Surono, Jousset P., Pallister, J., Boichu, M.M., Buongiorno, F., Budisantoso, A., Costa, F., Andreastuti, S., Prata, F., Schneider, D., Clarisse, L., Humaida, H., Sumarti, S., Bignami, C., Griswold, J., Carn, S., Oppenheimer, C., Lavigne, F. (2012). The 2010 explosive eruption of Java's Merapi volcano—A '100-year' event. Journal of Volcanology and Geothermal Research, Volumes 241–242, Pages 121-135, DOI: 10.1016/j.jvolgeores.2012.06.018.

Taylor, S.R. and McLennan, S.M. (2009) Planetary Crusts: Their Composition, Origin and Evolution. Cambridge University Press, Cambridge.

Thorpe, M. T., Hurowitz, J. A., & Dehouck, E. (2019). Sediment geochemistry and mineralogy from a glacial terrain river system in southwest Iceland. Geochimica et Cosmochimica Acta, 263, 140-166.

Thuleau, S., & Husson, F. (2017). FactoInvestigate: Automatic Description of Factorial Analysis. R Package Version, 1.

Treiman, A. H., Bish, D. L., Vaniman, D. T., Chipera, S. J., Blake, D. F., Ming, D. W., Morris, R. V., Bristow, T. F., Morrison, S. M., Baker, M. B., et al. (2016), Mineralogy, provenance, and diagenesis of a potassic basaltic sandstone on Mars: CheMin X-ray diffraction of the Windjana sample (Kimberley area, Gale Crater), J. Geophys. Res. Planets, 121, 75– 106, DOI: 10.1002/2015JE004932.

Udry, A., Gazel, E., and McSween, H. Y. (2018). Formation of evolved rocks at Gale crater by crystal fractionation and implications for Mars crustal composition. Journal of Geophysical Research: Planets, 123, 1525– 1540, DOI: 10.1029/2018JE005602

Vaissie, P., Monge, A., & Husson, F. (2015). Factoshiny: Perform factorial analysis from FactoMineR with a shiny application. R Package Version, 1.

Vaniman et al. (2014). Mineralogy of a Mudstone at Yellowknife Bay, Gale Crater, Mars. Science, Vol 343, Issue 6169. DOI: 10.1126/science.1243480

Voight, B., Constantine, E.K., Sismowidjoyo, S., Torley, R. 2000. Historical eruptions of Merapi Volcano, Central Java, Indonesia, 1768–1998. Journal of Volcanology and Geothermal Research 100, 69–138, DOI: 10.1016/S0377-0273(00)00134-7.

Wahyuni, E. T., Triyono, S., Suherman. 2012. Determination of Chemical Composition of Volcanic Ash from Merapi Mt. Eruption. Journal of People and Environment, vol. 19, no. 2, 1 Jul. 2012, pp. 150-159, DOI: 10.22146/jml.18531.

Wei, T., & Simko, V. (2017). R package 'corrplot': Visualization of a correlation matrix (version 0.84). Retrieved from Https://Github. Com/Taiyun/Corrplot.

Wickham, H. (2017). Tidyverse: Easily install and load 'tidyverse' packages. R Package Version, 1(1).